Fusion Engineering and Design 198 (2024) 114087

Contents lists available at ScienceDirect

Fusion Engineering and Design

journal homepage: www.elsevier.com/locate/fusengdes

Shape manipulation of a rotating liquid liner imploded by arrays of pneumatic pistons: Experimental and numerical study

Nicholas S. Mangione [1,*], Hao Wu, Claire Preston [1], Anthony M.D. Lee [1], Sohrab Entezami, Raphaël Ségas [1], Piotr W. Forysinski [1], Victoria Suponitsky [1]

General Fusion Inc., 3680 Bonneville Pl, Burnaby, BC V3N 4T5, Canada

ARTICLE INFO

Keywords:
MTF
Liner implosion
Free surface
Implosion shaping
Piston
OpenFOAM

ABSTRACT

Shaping the inner surface of a rotating, imploding liquid metal liner as it compresses a magnetised plasma target is an important aspect of the Magnetised Target Fusion (MTF) scheme pursued by General Fusion. Reduced-order modelling has shown that the liner's inner surface shape can be manipulated during the implosion by spatially varying the amplitude and timing of pressure applied at the liner's outer surface. A sub-scale apparatus was constructed to investigate this concept, using water as the liner material. A simplified axisymmetric model of this apparatus was also developed using OpenFOAM software. Experimental pressure and rotational speed were used as inputs to numerical simulations. Very good agreement between numerical and experimental liner trajectories was obtained for a wide range of implosion parameters. Data analysis confirmed an initially cylindrical inner liner surface can be shaped and the shaped surface remains symmetrical to radial compression ratios of at least 7:1, despite driving the implosion using pneumatic piston arrays. Furthermore, experiments demonstrated suppression of Rayleigh-Taylor instability for shaped implosions by using liner rotation. This is significant, as literature only confirms this suppression for cylindrical implosions. These results increase confidence in simplified numerical modelling as a predictive tool for designing MTF machines.

1. Introduction

The main objective of this experimental and numerical work is to provide a solid proof of concept for the design and construction of the plasma compression system for a Magnetised Target Fusion (MTF) scheme being pursued by General Fusion [1,2]. In this scheme, a magnetised plasma is injected into a vacuum cavity inside a rotating liquid metal liner, which is then imploded using highly pressurised gas that actuates arrays of pneumatic pistons. As the liner implodes, it compresses a magnetised target plasma to thermo-nuclear conditions. A schematic of General Fusion's Fusion Demonstration Prototype (FDP) is shown in Fig. 1a and details about the MTF scheme can be found in the following Refs. [2–6]. The success of this MTF scheme relies on two major components, which to a large extent can be studied independently. The first component is the formation of a magnetised plasma target and its interaction with the liquid metal liner [7,8]. The second, which is the focus of the current work, is an apparatus (known as the compression system) to form and subsequently implode a liquid liner in a way that is effective for plasma compression [7,9–14].

The design of the compression system for the FDP [15] is based on the results of extensive numerical modelling and sub-scale experimental test beds, which have been used to examine a variety of compression schemes and sub-systems [3,12,13,16–20]. To achieve effective plasma compression, it is important to ensure high symmetry and smoothness of the plasma-facing liquid metal liner surface during the implosion. Various types of interface instabilities, such as Bell-Plesset, Kelvin--Helmholtz, Rayleigh-Taylor, and magnetic Rayleigh-Taylor may potentially develop during implosion of the liner [17,18,21–25]. This may cause contamination and cooling of the plasma, resulting in reduced compression efficacy.

During the implosion, the inner surface of the liner is initially accelerated inwards, *i.e.*, the heavier fluid accelerates into the lighter one. During this phase, the inner surface is Rayleigh-Taylor stable, but perturbations undergo a slow oscillatory growth because of the converging geometry, known as Bell-Plesset effects. To minimise the amplitude of surface perturbations during the inward acceleration

* Corresponding author.
E-mail address: nicholas.mangione@generalfusion.com (N.S. Mangione).
[1] Present address: General Fusion Inc., 6020 Russ Baker Way, Richmond, BC V7B 1B4, Canada.

https://doi.org/10.1016/j.fusengdes.2023.114087
Received 31 July 2023; Received in revised form 24 October 2023; Accepted 28 November 2023
Available online 12 December 2023

phase, it is important for the liner surface to be smooth and symmetrical prior to implosion. Deep into compression, the inner surface starts to decelerate until it reaches maximum compression and turns around. This deceleration is caused by increased pressure of the gas (plasma) target, and, in the case of a rotating liner, by the centrifugal force. In the absence of rotation, the light fluid pushes on the heavier one during deceleration phase leading to the onset of Rayleigh-Taylor instability. In the case of a rotating liner, the centripetal acceleration at the inner surface may be sufficient for the total acceleration to remain inward (negative) during the entire implosion, and, therefore, to prevent the

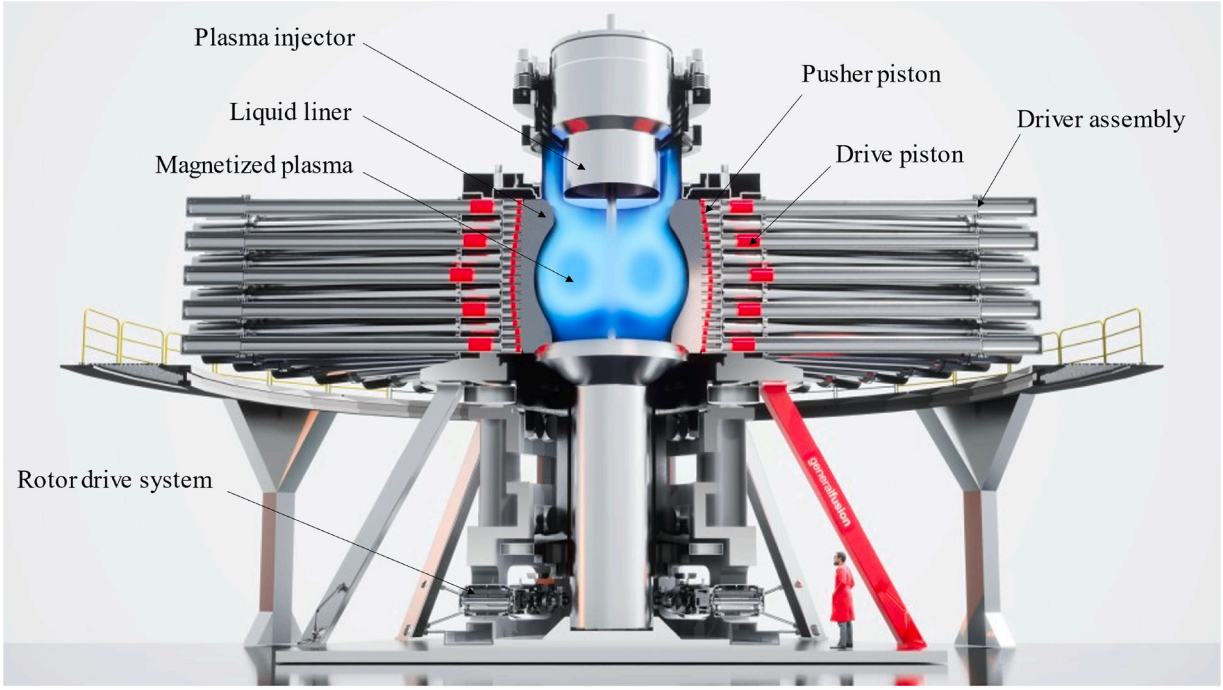

(**a**)

(**b**)

Fig. 1. (**a**) Rendering of the Fusion Demonstration Prototype (FDP) being designed by General Fusion to demonstrate Magnetised Target Fusion (MTF) technology. (**b**) 1/10th scale prototype of the FDP compression system used to study liner implosions. It is known as the Cylindrical Water Compressor (CWC) because it uses water as the working fluid.

onset of Rayleigh-Taylor instability. For cylindrical implosions, rotational stabilisation of Rayleigh-Taylor instability was investigated in the following theoretical and experimental studies [23–27]. In a computational study, [28] it was also demonstrated that rotation suppresses growth of the mixing zone originated by Rayleigh-Taylor instability. For a comprehensive review about Rayleigh-Taylor and other hydrodynamic interface instabilities, see recent papers [29–31].

It should be emphasised that General Fusion's compression scheme heavily relies on suppression of Rayleigh-Taylor instability by sufficient initial rotation of the liner. As such, experimental parameters for the current study are chosen to satisfy the criterion for rotational stabilisation (negative total acceleration [23–27]), and hence, for cylindrical implosions, the inner surface of the liner is expected to remain Rayleigh-Taylor stable at all times. The criterion is experimentally confirmed only for cylindrical implosions, but numerical simulations indicate that it is also possible to suppress Rayleigh-Taylor instability in the case of a shaped liner, at least for the cases being considered. An experimental confirmation of Rayleigh-Taylor stable implosions for shaped liners is vital for increased confidence in the results of these numerical simulations. It is important to reiterate that even when exponentially growing Rayleigh-Taylor instability is fully suppressed by rotation, there is still slow perturbation growth due to convergence (Bell-Plesset), hence, minimising surface perturbations on the inner surface of the liner prior to implosion is of utmost importance.

Based on previous work it has been concluded that the most robust method to form an initially smooth liner surface is by solid body rotation [21,23–25]. This can be achieved by rotating the inner part of the apparatus, known as the *rotor*, and shown as the housing of the innermost red pistons in Fig. 1a. The rotor is a hollow cylinder whose outer annulus contains horizontal layers of discrete, radially oriented round piston bores. Prior to implosion, liquid is retained inside the rotor by *pusher* pistons, which can freely slide inside their bores but have their radial displacement limited by mechanical stops. A layer of liquid resides in front of the inner surface of the pusher pistons, and its thickness is sufficient to minimise surface perturbations at the initial stage of the implosion [21,25,32–34].

To compress a magnetised plasma target in the desired manner, it is essential to shape the initially nearly cylindrical inner surface of the liner during the implosion [35,36]. It has been predicted by in-house numerical modelling that the shape can be manipulated by tuning the timing and amplitude of external pressure applied to the pusher pistons in each of the horizontal layers [13,37,38]. Experimental confirmation that the shape of the liner's inner surface can indeed be controlled by this method is important for the success of the MTF scheme.

In practice, one way to manipulate pressure applied to the pusher pistons is to surround the rotor with a second stationary array of pneumatically driven pistons arranged into horizontal layers, each capable of operating independently. Upon launching these outer *drive* pistons, gas in front of them is pressurised, and acts upon the outer surface of the rotor. This causes the pusher pistons to move inwards, ejecting liquid out of their bores to form an imploding, rotating liquid liner.

To de-risk the proposed compression scheme, a 1/10th scale version of the FDP compression system was constructed at General Fusion. The machine is known as the Cylindrical Water Compressor (CWC) and is depicted in Fig. 1b. *Cylindrical* refers to the geometry of the rotor, *Water* stands for the principal working fluid (see Section 2.2.2 for details), and *Compressor* relates to the compression of the gaseous cavity by an imploding liner.

This paper summarises experimental results obtained with the CWC and how they compare to simplified numerical modelling. CWC experiments have been running for over two years and hundreds of liner implosions (*shots*) have been performed over a broad range of operating parameters. The six shots presented in this study were selected based on the main goals set to de-risk the compression scheme for the FDP. These goals are: (i) achieving symmetrical implosions with a smooth inner surface of the liner up to at least 7:1 radial compression ratio using discrete pistons, (ii) controlling the shape of the inner surface of the liner by tuning the amplitude and timing of pressure applied to its outer surface, and (iii) suppressing Rayleigh-Taylor instability at the inner surface by sufficient initial rotation of the liner. The size of the CWC and its de-risking goals were set by balancing the cost of the sub-scale apparatus and the need to operate in a regime relevant to the FDP, such that key compression scheme challenges could be identified early on.

The rest of the paper is organised as follows. In Section 2, descriptions of the experimental apparatus (2.1), diagnostics (2.2) and experimental procedures (2.3) are provided. The numerical modelling methodology is described in Section 3. Analysis of six selected compression shots is given in Results and Discussion (Section 4) and finally conclusions are presented in Section 5.

2. Apparatus, diagnostics, and methods

2.1. Experimental apparatus

A section-view CAD model of the CWC is shown in Fig. 2a, and detailed views of its sub-components are provided in parts 2b-2e. The liquid metal liner shown in the schematic of the FDP (see Fig. 1a) is replaced by the aqueous one which is denoted as *liquid liner* in Fig. 2a. The rotor assembly is shown in Fig. 2b. Detailed views of the driver and pusher assemblies are provided in Fig. 2c and 2d, respectively. For simplicity, driver assemblies are only shown on the right-hand side of the CAD model, but in reality, they are present all around the machine as shown in Fig. 1b. Fig. 2e depicts typical installations of gap pressure sensors and PDV diagnostic ports (see Section 2.2.1). Key dimensions and parameters of the system are listed in Table 1.

Similar to the FDP, the CWC comprises a rotor and a surrounding stationary vessel. The rotor, which is a hollow cylindrical structure (see Fig. 2b), is spun by a fifteen-horsepower electric motor mounted underneath the vessel. Both rotor and vessel are sectioned into seven horizontal layers, referred to as layers A-G (bottom to top, Fig. 2a) throughout the manuscript. Each layer of the rotor comprises 21 pusher bores. Inside each pusher bore there is a pusher piston that is free to move radially. When the rotor is spinning and filled with water, pusher pistons reside near its outer surface and are held by end stops located inside the bores. If the pressure acting on the outer surface of the rotor, referred to as *gap pressure* throughout the manuscript, exceeds a certain threshold imposed by the force balance on the piston (see Section 4.1.1), the pusher pistons move inwards. Liquid is then ejected from the bores to initiate liner implosion. An end stop also exists at the inner end of the pusher bore to prevent pistons from leaving the bore. Under typical initial conditions, there is a layer of liquid in front of the inner surface of the rotor, *i.e.,* the initial radius of the cavity is smaller than the inner radius of the rotor, and the liquid and rotor are in solid body rotation. The shape of the free surface, which is referred to as the *inner surface of the liner*, initially deviates from a cylindrical one because of gravity and is a circular paraboloid instead [39] (see Fig. 2a and Section 3 for further details).

To fill the rotor with water and to set an initial gas pressure inside the cavity, liquid and gas connections are provided through axial access ports located at the top and bottom of the rotor *via* the laser plane diagnostic hardware (see Section 2.2.2 for details). The liquid and gas connections are automatically closed by solenoid valves (not shown in Fig. 2) just prior to an implosion.

As previously discussed, the liner is imploded by the buildup of gap pressure acting upon pusher pistons. This gap pressure is generated by an array of driver assemblies mounted onto the stationary vessel which surrounds the rotor. The CWC comprises seven horizontal layers of driver assemblies (see Fig. 2c), which operate independently. There are 36 circumferentially distributed driver assemblies per layer, for a total of 252.

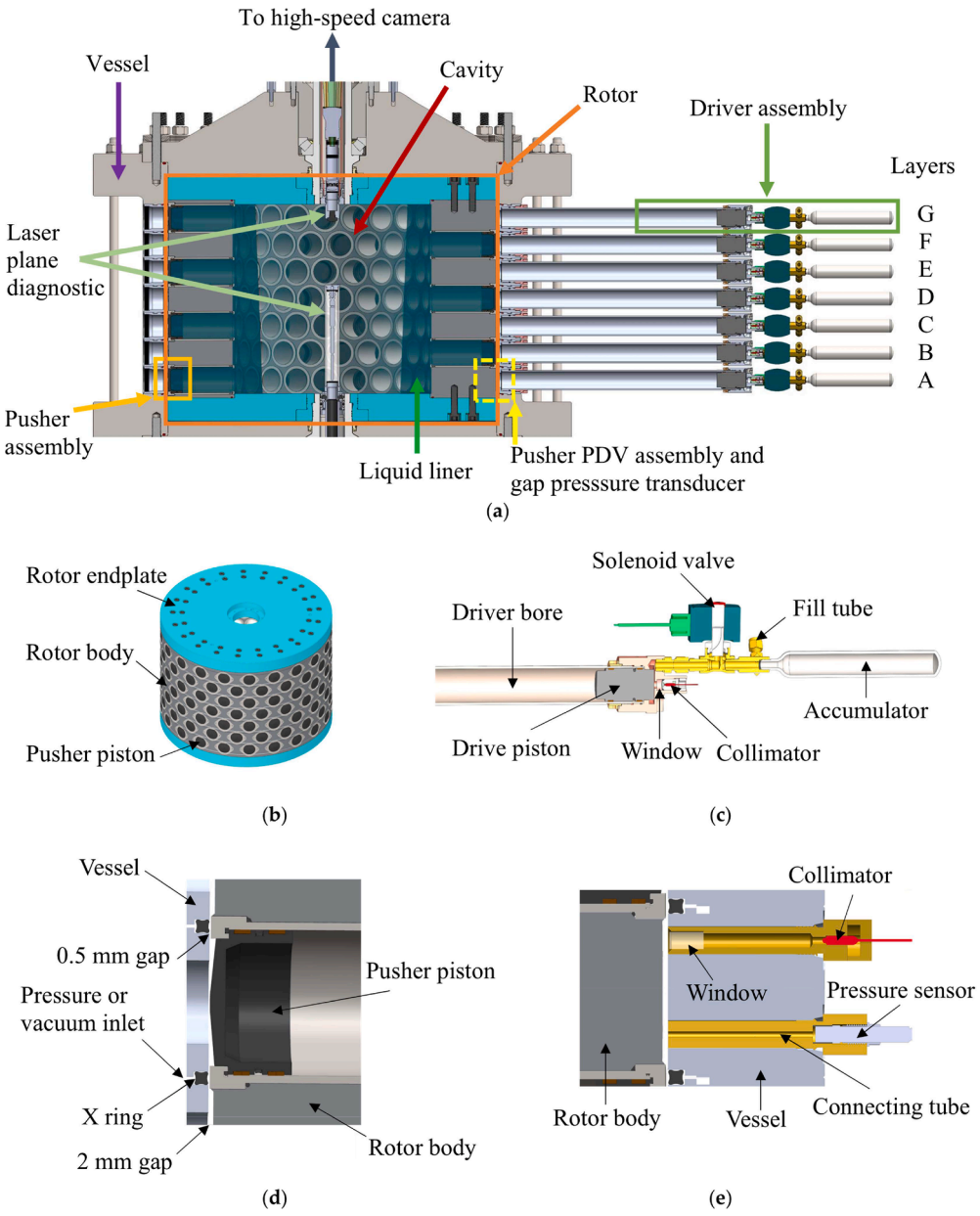

Fig. 2. CWC (photograph presented in Fig. 1b) CAD model and sub-components. (**a**) Cross-section view of the CWC with rotor, diagnostics, and a representative column of driver assemblies shown on the right-hand side. (**b**) Isolated view of rotor. (**c**) Cross-section view of driver assembly. (**d**) Cross-section view of pusher piston assembly and sealing system. (**e**) Cross-section view of pusher piston photonic Doppler velocimetry (PDV) collimator assembly and pressure transducer insert. These inserts are on a section plane other than shown in (a), azimuthally bisecting the spacing of the driver bores.

Each driver consists of an accumulator (Leland 89075 75 g cylinder) to store pressurised nitrogen, a solenoid valve (ASCO 8262H212), a drive piston, and its bore. All driver accumulators within each horizontal layer are connected to ensure that they are pressurised equally. Each solenoid valve is actuated by a custom-built high-voltage power system which controls valve opening time to a high degree of precision, typically 0.05 ms.

There is a small air gap (see Fig. 2d) between the rotor and the vessel, which is referred to as the *gap* in this paper. The width of the gap varies in the axial direction. On the one hand, circumferential flow sharing within each layer (*intra-layer*) is desired to facilitate a symmetrical implosion and, thus, a wider gap width of 2 mm is employed. On the other hand, to vary gap pressure in the axial direction, flow sharing between horizontal layers needs to be minimised and, hence, the *inter-layer* gap width between adjacent layers is reduced to 0.5 mm, a minimum dictated by engineering constraints.

In this work, two types of implosions are considered. The first employs identical accumulator pressures and valve opening times for all horizontal layers, and the second employs accumulator pressures and/or valve opening times which vary from one horizontal layer to the next. In this manuscript these are referred to as *cylindrical implosions* and *shaped implosions*, respectively.

For shaped implosions, to further minimise inter-layer gap pressure equalisation, an actuated sealing mechanism is incorporated between the rotor and the vessel (see Fig. 2d). Actuated seals are located between each adjacent layer as well as above and below the top and bottom layers (G and A), respectively. Each seal comprises an x-ring (5.5 mm in cross section) held in a groove in the vessel wall at the location of minimum gap width, whose diameter can be changed by differential gas pressure. Eight accumulators and solenoid valves, identical to those employed in the driver assemblies, propel the x-rings onto the rotor's outer surface, creating a temporary seal between rotor and vessel. When not engaged,

Table 1
Key parameters of the Cylindrical Water Compressor (CWC).

Part name	Parameter	Value
CWC	Number of driver (horizontal) layers	7
	Number of drive pistons per layer	36
	Number of pusher pistons per layer	21
	Number of pusher layers per driver layer	1
Rotor	Inner radius	0.2164 m
	Outer radius	0.3615 m
	Inner height	0.4200 m
	Outer height	0.5400 m
	Nominal initial cavity radius	0.1500 m
Diagnostics	Laser plane diagnostic shaft radius	0.0150 m
Pusher assembly	Pusher bore radius	0.0286 m
	Pusher piston radius	0.0285 m
	Pusher piston length	0.0323 m
	Pusher piston stroke	0.1108 m
	Pusher piston mass	0.118 kg
Driver assembly	Driver bore radius	0.0197 m
	Drive piston radius	0.0189 m
	Drive piston length	0.0650 m
	Drive piston stroke	0.4879 m
	Drive piston mass	0.419 kg
	Accumulator volume	1.02×10^{-4} m^3
Gap	Inter-layer radial gap — rotor to vessel	0.0005 m
	Intra-layer radial gap — rotor to vessel	0.0020 m

the volume behind each x-ring is evacuated, which draws the x-ring back into the groove and disengages it from the rotor. These seals are only engaged when necessary to reduce their wear, minimise heat generation, and to avoid excessive drag on the drive system.

2.2. Diagnostics

2.2.1. Sensors

In this study, two different types of measurements are employed: (i) pre-implosion steady-state ones, such as initial accumulator and cavity pressures, and (ii) time-dependent measurements during the implosion, such as gap pressure for each horizontal layer. Different sensors are used for each type of measurement. Pressure in the cavity prior to the implosion, referred to as *initial cavity pressure* throughout the manuscript, is measured using a Honeywell 19C030PA4K pressure sensor. Initial accumulator pressures are set and measured with Proportion-Air QB1SANEEZP300PSG electronic pressure regulators. Time-dependent gap pressure of each of the seven layers is measured using seven PCB Piezotronics model 113B24 ICP pressure sensors (Fig. 2e). A custom-built tachometer system is implemented using a disk with 84 slots to measure the rotational speed of the rotor before and during implosion. The velocity of a subset of pusher and drive pistons is measured with a 36-channel, 1550 nm photonic Doppler velocimetry (PDV) [40] system. PDV laser collimator assemblies for velocity measurements of drive pistons and pusher pistons are shown at representative locations in Fig. 2c and 2e, respectively. Time dependent gap pressure and rotor speed as well as the initial cavity pressure are used as inputs for

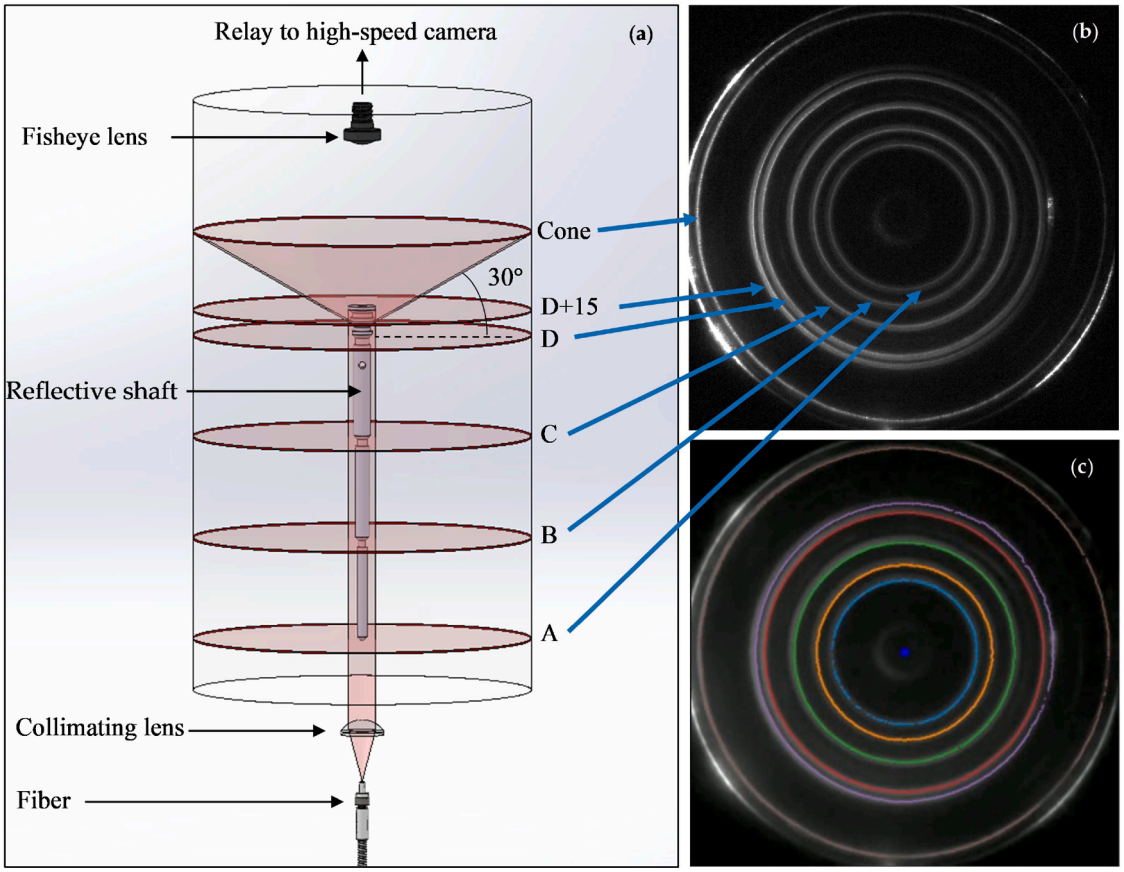

Fig. 3. (**a**) Schematic of the laser plane diagnostic (LPD). The setup consists of a fibre-coupled laser source expanded with a collimating lens. The laser impinges upon a machined shaft with polished surfaces, generating laser planes and a cone. Labels A, B, C, D correspond to laser planes nominally located at the axial midpoints of the A, B, C, and D piston layers. D+15 is located 15 mm above D, and the cone is elevated 30° above horizontal. Both D+15 and the cone illuminate the liner above the equator. A fisheye lens, whose image is optically relayed to a high-speed camera, is used to capture video of the laser planes and cone diffusely reflecting off the liner. (**b**) Frame from a high-speed video of the LPD with the laser planes and cone identified. The outermost ring (unlabelled) is a specular reflection from the liner. (**c**) Colour overlay of the laser planes and cone detected by the image processing algorithm on top of the frame in (b).

numerical simulations (see Section 3 for details).

2.2.2. Laser plane diagnostic

A structured light system, called the Laser Plane Diagnostic (LPD), was developed in-house to measure the position of the liquid liner throughout the experiment. The LPD is shown schematically in Fig. 3. It comprises an illumination apparatus and an imaging apparatus, inserted respectively through axial access ports at the bottom and top of the CWC (see Fig. 3a).

The illumination apparatus projects a pattern onto the liner's inner surface. This pattern is created by expanding a 10 W 635 nm (red) fibre-coupled laser to a 16 mm diameter collimated beam that enters the CWC from the bottom diagnostic access port and is directed axially upward. The laser beam impinges upon a precision machined aluminium 7075 shaft suspended within, and protected by, a transparent cast acrylic tube (not shown in Fig. 3a). The aluminium shaft has six mirror-polished conical frustums with increasing radii from bottom to top. These conical surfaces reflect the laser toward the inner surface of the liner as shown in Fig. 3a. Five of the frustums have cone angles of 45° and reflect the incident light into horizontal laser *planes* at nominal heights of 30, 90, 150, 210, and 225 mm above the rotor floor. These are labelled as A, B, C, D, and D+15, and correspond to the midpoints of the A, B, C, and D piston layers, and 15 mm above the mid-point of layer D, respectively. Laser plane D corresponds to the mid height, or *equator*, of the 420 mm rotor. The sixth frustum creates a laser *cone* angled upward at 30° above horizontal (see Fig. 3a). The purpose of the sixth frustum is to measure the position of the inner surface of the liner above laser plane D+15. Using the cone avoids the need to extend the height of the LPD, which would occlude the view of lower layers at small liner radii. Laser plane D+15 and the cone were added later in the testing campaign and were not available for all the shots presented in this work.

To promote diffuse scattering of the red laser light from the liner surface, and to suppress subsurface scattering, a coolant emulsion (Cimcool Cimperial 1070) of 5 % v/v in water is used as the working fluid. Subsurface scattering is further suppressed by colouring the emulsion with blue and green food dyes to absorb the red laser light. For simplicity, the working fluid is referred to as water throughout the text.

To capture images of the laser planes and cone, a 180° fisheye lens (Sunex DSL219) is mounted 35 mm below the ceiling of the rotor facing axially downward. The image from this fisheye lens is relayed by a pair of optical relays to a high-speed monochrome camera (Photron Fastcam Nova S12), which is mounted above the CWC. Both the illumination and imaging apparatuses are secured to the vessel and are stationary relative to the rotor. To achieve this, they are fitted with bearings, as well as seals which isolate the cavity from the atmosphere. The camera captures high speed video at 10,000 fps with a resolution of 1024 × 1024 pixels, using an exposure time of 50 μs.

2.3. Procedures

2.3.1. Laser plane and cone calibration

The positions of the laser planes and cone were calibrated by inserting the illumination apparatus into the CWC with the rotor removed. The axial positions of the peak intensities of the laser planes and cone were measured using metric grid paper at six azimuthal positions and two different radii. As azimuthal variation was determined to be small (approximately ±0.5 mm), all azimuthal measurements at each radius were averaged and linear interpolation was used to determine the position of the laser planes and cone at other radii within the cavity.

2.3.2. Camera calibration

Calibration of the LPD imaging apparatus (fisheye lens, optical relays, and camera) to map radial and axial coordinates within the rotor was performed outside the CWC. In summary, a radial checkerboard calibration pattern was imaged at several discrete distances (heights) from the camera, covering the full extent of the liner surface viewed by the fisheye lens. A calibration surface was constructed by relating the axial height from the rotor floor, z, radial coordinate r in meters, and corresponding image radial coordinates in pixels r_{pix}. Additional description of the calibration procedure is provided in Supplementary Material Section S1.

2.3.3. Inner liner surface analysis

With the calibrated positions of the laser planes and cone, there is 1:1 mapping between an identified laser reflection's radius in camera pixels and its 3D spatial position. Thus, once a laser plane or cone is identified in the video, the camera calibration can be used to determine the position of the liner surface. A typical frame from a high-speed video of the LPD shortly after the pusher pistons have been launched is shown in Fig. 3b. At this point in the implosion, the inner surface of the liner is nearly cylindrical, and, thus, it is easy to identify the A, B, C, D, D+15 planes and cone as they are all visible and ordered radially outwards.

A custom algorithm was developed to extract the laser plane and cone reflections from the high-speed video, track them during the shot, and use the camera and LPD calibrations to perform 3D reconstruction of the liner surface shape. A detailed description of the process is provided in Supplementary Material Section S2. Under certain conditions, some lower plane reflections are occluded by the liner due to its convex shape. In addition, during deep implosions, laser planes A and B are occluded by the mounting hardware of the reflective shaft. The tracking of these planes resumes once the liner moves outwards and their reflections come back into view. The intensity of the laser reflections may vary with azimuthal angle and sometimes fall below a detection threshold, resulting in gaps in the data. For each of the laser planes and cone, liner trajectories, presented in subsequent sections of this manuscript, were obtained by averaging the liner's radial position in the azimuthal direction.

The initial cavity radius is determined from the laser plane measurements of the liner surface position prior to implosion. Details of this procedure are provided in Section 3. The initial cavity radius could also be calculated from the volume of liquid pumped into the system. This method, however, was found to be less accurate due to uncertainty introduced by the fill piping.

Standard error propagation methods were used to estimate error in the radial position of the liner. This was done by estimating uncertainties introduced by the following: the optical calibration pattern vertical and radial misalignment and tilt (±1 mm, ±1 mm, ±0.5°); the laser plane diagnostic shaft vertical and radial misalignment and tilt (±0.5 mm, ±1 mm, ±0.5°); the imaged laser line full-width-half-maximum (±5 pix); and the optical calibration surface interpolation. It is worth noting that fisheye lens distortion causes larger uncertainties at the edges of the camera field of view and magnifies effects of misalignment.

2.3.4. Cylindrical implosion procedure

For a cylindrical implosion, wherein the liquid liner maintains its quasi-cylindrical shape, the rotor was first spun at the nominal initial rotational speed, Ω_0, and then filled with water. The gaseous cavity within the rotor was evacuated to the specified initial pressure. All accumulators were filled with nitrogen gas to the same pressure and all solenoid valves were actuated simultaneously. Initial measurements of pressures and rotor speed (see Section 2.2.1) were taken immediately prior to driver solenoid actuation. For all cases presented in this study, data acquisition started at $t = 0$ and was synchronised across all sensors and diagnostics. Solenoid valve actuation occurred at $t = 40.1$ ms. After the shot, the cavity and the gap were vented to atmosphere in preparation for subsequent implosions. At this point, the rotor speed and cavity pressure were reset, and vacuum was applied to the volume behind the drive pistons, pulling them back to their initial positions.

Liner fluid density was measured manually after each series of shots and used as an input parameter for simulation. Three samples were collected after each series and the density was found to vary by less than

1 %.

2.3.5. Shaped implosion procedure

In contrast to the cylindrical implosion, a shaped implosion is achieved by varying both accumulator pressures and valve actuation times between the horizontal layers, or by varying accumulator pressures only. To achieve the desired axial distribution of gap pressure, engagement of the inter-layer seals was required (see Section 2.1). These seals were actuated at $t = 0.1$ ms. Shortly after a shot, the x-rings were retracted *via* a vacuum system, which readies the machine for another implosion. The remainder of the shaped implosion procedure is similar to that of the cylindrical implosion.

3. Computational methodology

Simulations of liquid liner implosions were carried out using the 'compressibleInterFoam' solver, which is part of the open-source C++ libraries of OpenFOAM software [41]. 'compressibleInterFoam' is a multiphase solver which uses a Volume of Fluid (VoF) phase-fraction-based interface-capturing approach to model two compressible, immiscible fluids. The momentum and other fluid properties are of the 'mixture', *i.e.,* properties vary according to the volume fraction of each phase, and a single momentum equation is solved. A complete set of governing equations for 'compressibleInterFoam' solver can be found in [42] and in the Appendix of [18]. The overall numerical procedure is an extension of the one used in the 'interFoam' solver, which is described in great detail in [43,44]. In this work, the 'OpenFOAM 10' version released by CFD Direct was used. For the range of parameters considered in this study, the liquid phase can be modelled as incompressible, whereas the gas phase is highly compressible, hence a compressible solver is used. The 'compressibleInterFoam' solver has been used extensively to simulate liquid liner implosions and has been found to robustly capture interface dynamics including interface instabilities [3,17,18,25].

This computational study is limited to simulating the rotating part of the CWC, *i.e.,* the computational domain extends radially up to the outer surface of the rotor. The stationary part of the machine, *i.e.*, driver assembly in Fig. 2c, is left for future work. To decouple the rotating part from the rest of the apparatus, experimentally measured gap pressures (see Section 2.2.1) are applied as a boundary condition at the pusher pistons.

By isolating the rotating part, it is easier to examine assumptions and simplifications of a computational model, because the uncertainty associated with the simulation of gas flow between the accumulator and the outer surface of the rotor is eliminated. The objective is to test a simplified model to predict the overall dynamics of the liquid liner in a complex, three-dimensional apparatus. The computational model is intended to be general and computationally *light*, but capable of providing robust predictions to a desired level of accuracy. Assumptions and simplifications made in this work are outlined below.

The first simplification is reducing the dimensionality of the problem from 3D to 2D axisymmetric. By doing so, it is assumed that key characteristics of liner implosions, such as the shape of the inner surface and its trajectory, are not sensitive to the particular arrangement of pusher bores inside the rotor. In the 2D axisymmetric setup, each horizontal layer of discrete circular pusher bores is represented by an annular slit. The height of the slit varies in the radial direction such that its area is consistently equal to the sum of the cross-sectional areas of all the pusher bores in a single layer.

The second simplification is removing the solid pusher piston from the simulation setup. This avoids simulating moving parts and reduces geometrical complexity, which results in a significant decrease in computational cost. To account for the mass of the pusher pistons, extra liquid is added to each of the annular slits. The mass of the additional liquid is equal to the sum of the pusher piston masses in each horizontal layer. This way of modelling the pistons changes the total angular momentum of the system. The change is estimated to be on the order of 1 %, and, therefore, no meaningful alteration of the liner dynamics is expected. Another implication of modelling the pistons as additional liquid is that the driving gas is now pushing directly on a liquid surface (instead of a solid). This may cause distortion of the liquid-gas interface due to the onset of the Rayleigh-Taylor instability, which does not happen in the experimental apparatus.

Lastly, small geometrical features, such as end stops inside the pusher bores, are omitted at this stage. The effect of these end stops on the overall liner dynamics is assumed to be minor, although they do influence the flow field structure locally. As the experimental apparatus evolves, those small features are often modified, and thus it is beneficial to have a general model if it is adequate.

A schematic of the computational setup is shown in Fig. 4, where part (a) depicts the initial state and boundary conditions, and part (b) shows an instant during implosion.

OpenFOAM software is intrinsically 3D, and 2D axisymmetric geometry is simulated using a wedge computational domain (5 degrees in this study) which is one cell thick in the azimuthal direction. A special *wedge* boundary condition is applied to the wedge planes, which is an equivalent to a *cyclic* boundary condition used in 2D problems (see OpenFOAM manual for details [41]).

The computational domain comprises a hollow cylinder which radially extends from the outer edge of the laser plane diagnostic shaft to the outer surface of the rotor. Axially, its size is equal to the inner height of the rotor (see Table 1). Seven annular slits, denoted by letters A to G, correspond to the horizontal layers of discrete pistons. In the radial direction, width $w(r)$ of the slit varies according to Eq. (1):

$$w(r) = n_{\text{pusher}} \pi R_{\text{pusher}}^2 \Big/ (2\pi r), \tag{1}$$

where n_{pusher} is the number of pusher pistons in a horizontal layer and R_{pusher} is the radius of the pusher piston (see Table 1). The radial extent of the annular slit is equal to the sum of the radius of the rotor's outer surface and the length of the additional liquid, l_{pusher}, which is used to account for the pusher piston. The length of the additional liquid is calculated by Eq. (2):

$$l_{\text{pusher}} = \frac{m_{\text{pusher}}}{\rho_{\text{liquid}} \pi R_{\text{pusher}}^2} \tag{2}$$

where m_{pusher} is the mass of each pusher piston and ρ_{liquid} is the density of the working fluid. For the parameters in Table 1 and the reference density $\rho_{\text{liquid}} = 1050$ kg/m^3, $l_{\text{pusher}} = 0.044$ m.

Pressure as a function of time is prescribed at the slit entrances using experimental gap pressures for each horizontal layer (denoted in Fig. 4a by $p_A(t)$, *etc.*). Experimental pressure data have been pre-processed before being applied in simulations; see Appendix A for details. The gaseous phase (pushing gas) was prescribed by using a fixed value boundary condition at the slit inlets. A slip wall boundary condition was used for all walls inside the computational domain. Simulations were run on a structured quasi-uniform mesh with a cell size of 0.6 mm. This grid resolution was found sufficient to produce grid-independent results. The Tait equation of state [45] was used for the liquid phase. No turbulent modelling was applied.

Prior to implosion, all the liquid inside the apparatus is assumed to be in solid body rotation. The azimuthal velocity component is thus initialized as $v_\theta = \Omega_0 r$, where Ω_0 is the initial rotational speed of the rotor and r is the radial coordinate. The radial and axial velocity components are initially zero. The rotor speed does not remain constant during the experiment. The rotor decelerates as the inter-layer seals are engaged and accelerates as liquid is pushed out of the bores. It is assumed that rotational velocity of the liquid inside the pusher bores is always equal to the rotor speed. Therefore, during the simulation, the azimuthal velocity component of the liquid inside the pusher bores is prescribed as $v_\theta(t) = \Omega(t) r$, where $\Omega(t)$ is the instantaneous rotor speed

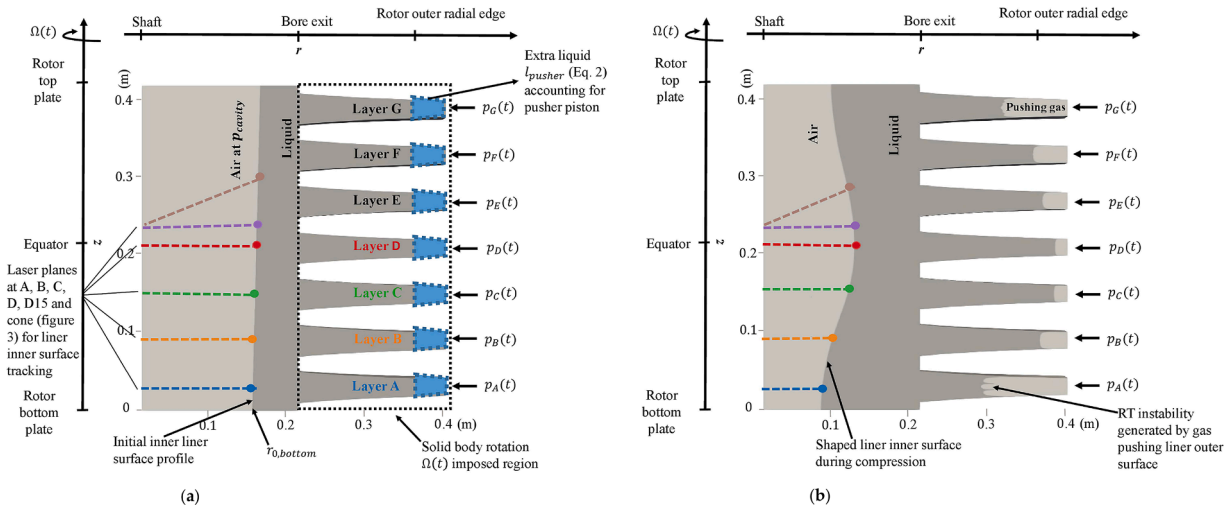

Fig. 4. A schematic of the computational setup for OpenFOAM simulations. (**a**) Computational domain with initial and boundary conditions. (**b**) Instantaneous flow field during the implosion, demonstrating the shaped inner surface achieved by varying pressures applied to horizontal layers.

as measured in the experiment (see Section 2.2.1). Rotor speed data are pre-processed similarly to the gap pressures; for details see Appendix A (Figs. A1–A5). The liquid in the bulk of the liner flows freely.

The initial shape of the liner's inner surface $r_0(z)$ is derived from hydrostatic equilibrium assuming solid body rotation, and is given by Eq. (3) [27,39]:

$$r_0(z) = \sqrt{\frac{2gz}{\Omega_0^2} + r_{0,\,\mathrm{bottom}}^2} \tag{3}$$

where g is gravitational acceleration, z is the axial coordinate, and $r_{0,\,\mathrm{bottom}}$ is the initial cavity radius at the bottom endplate of the rotor extrapolated from a parabolic fit to experimental data. Whilst gravity is taken into account to prescribe the initial shape of the inner surface of the liner, its effect on liner dynamics during implosion is neglected.

Hence, the pressure field in the liquid is initialised as:

$$p(r,z) = \frac{1}{2}\,\rho_{\mathrm{liquid}}\,\Omega_0^2 \cdot \left[r^2 - r_0^2(z)\right] + p_{\mathrm{cavity}} \tag{4}$$

which corresponds to liquid rotating as a solid body, where p_{cavity} is the initial gas pressure in the cavity. In each simulation, the initial cavity pressure and the density of the liner were set to the corresponding experimental measurements. All experimental data used as input for simulations are summarised in Table 2.

To compare liner trajectories obtained in experiments and simulations, the position of the liner surface was extracted at axial locations corresponding to the laser planes and cone in the apparatus (see Figs. 4a and 3).

For illustrative purposes, an instantaneous flow field during the implosion obtained with OpenFOAM is shown in Fig. 4b. One can see that an initially nearly cylindrical surface has been shaped due to variation in pressures applied to horizontal layers. It can also be seen that when pressure is applied and the liner moves inward, the volume behind the outer surface of the liquid pistons is now occupied by pushing gas. Finally, it is evident that the outer surface is distorted due to the onset of Rayleigh-Taylor instability.

Table 2
Experimental inputs for simulations.

Measurement	Pre-processing
Initial cavity radius	From parabolic fit to experimental data (Eq. (3) [27,39])
Initial cavity pressure	No
Initial liner density	No
Gap pressure	Filtering, truncation, and interpolation[1]
Rotor speed	Filtering, truncation, and interpolation[1]

[1] For details see Appendix A, Figs. A1–A5

4. Results and discussion

In this section, six selected cylindrical and shaped implosions are presented and discussed. These shots were chosen to address the main objectives of the CWC: (i) achieve symmetrical implosions with a smooth inner surface of the liner up to at least 7:1 radial compression ratio using discrete pistons, (ii) control the shape of the inner surface of the liner by tuning the amplitude and timing of pressure applied to its outer surface, and (iii) suppress Rayleigh-Taylor instability at the inner surface by sufficient initial rotation of the liner.

Parameters for all the cases considered are summarised in Table 3. The first column of the table lists the *shot numbers* (corresponding to the real experimental shot count), which are used as identifiers throughout this section. To target certain trajectories of interest, an in-house reduced order modelling code was first run to converge on a set of input parameters [37,38].

For the first five shots (#779, #777, #897, #898, #899), parameters were chosen such that the liner's inner surface reached a radial compression ratio of at least 5:1, while remaining RT stable throughout the entire compression [24,25]. Within the CWC's operational constraints, initial rotor speed (Ω_0), accumulator pressures ($p_{\mathrm{accumulator}}$), and initial cavity pressure (p_{cavity}) were then varied within a range that satisfied the above-mentioned requirements. This served as a broad experimental dataset for validation of numerical modelling. To get a rough estimate for the range of parameters which satisfy the criterion for rotational stabilisation, a reduced order in-house code modelling the entire system [37,38] was first run. Acceleration profiles were then analysed to identify a parameter space where total (radial + centripetal) acceleration, a_{total}, is negative during the entire implosion [24,25]:

$$a_{\mathrm{total}} = \frac{d^2 R_{\mathrm{mean}}(t)}{dt^2} - \Omega_R^2 R_{\mathrm{mean}}(t) < 0 \tag{5}$$

where $R_{\mathrm{mean}}(t)$ is the mean liner surface radius as defined in Section 4.1.3, but at a selected z (height) coordinate, and Ω_R denotes the liner surface rotation speed.

Experimental parameters were tuned to align with reduced order modelling. OpenFOAM simulations were then carried out using experimental gap pressures and acceleration profiles were extracted. Acceleration profiles for RT stable (#898) and RT unstable (#849) shots are

Table 3
List of parameters for the six selected shots analysed in this work.

Shot number	Shot type	Nominal rotor speed (rad/s)	Initial cavity pressure (kPa)	Accumulator pressure min-max (MPa)	Pusher piston end-stop collisions	Max. radial compression ratio ($C_{rad,\ max}$) at equator	Mean absolute deviation at $C_{rad,\ max}$ at equator (m)
779	Cylindrical	50.3	5.38	1.98 - 1.99	No	7.6:1	8×10^{-4}
777 * †	Shaped	50.3	5.45	0.99 - 2.16	Yes	7.2:1	6×10^{-4}
897	Shaped	57.1	5.45	1.17 - 1.81	No	5.2:1	3×10^{-4}
898	Shaped	57.1	5.45	1.19 - 1.91	No	5.7:1	2×10^{-4}
899	Shaped	45.0	8.00	0.89 – 1.72	Yes	5.7:1	11×10^{-4}
849	Cylindrical (RT unstable)	31.3	102.59	1.97 - 1.97	No	2.2:1	9×10^{-4}

* For shot 777 only, driver solenoid valve actuation time was varied between layers, $39.1 \leq t \leq 40.1$ ms.
† For shot 777, pusher pistons experienced higher static friction during launch because it was the first shot in its series.
The measured liquid density for all shots is (990 ± 10) kg/m^3.
For accumulator pressures used at each layer, please refer to Appendix B, Table 1.

shown in Fig. C1 in Appendix C to illustrate the criterion for rotational stabilisation.

In the last shot (#849), parameters were adjusted such that Rayleigh-Taylor instability is expected to develop at the inner surface of the liner at some point during the implosion. This was achieved by increasing p_{cavity} and decreasing both $p_{\text{accumulator}}$ and Ω_0. This shot was included to demonstrate that RT-stable and RT-unstable interfaces can be clearly distinguished.

Under certain operating conditions, pusher pistons in some of the horizontal layers may hit their inner end stops during the implosion. In this case, energy transfer from the pusher piston to the liner is interrupted at the time of collision. While not intended by design, these collisions were observed in some of the shots presented, as identified in Table 3. Further details on this are provided in Section 4.1.2.

It is also worth mentioning that static friction experienced by pusher pistons may vary depending on how recently they were last actuated. The shots were usually performed in series, and the first shot of each series was found to have higher static friction than subsequent ones. From the shots presented, #777 is the only one which was the first in its series, as noted in Table 3 and further discussed in Section 4.3.

For reference, key characteristics for each of the shots (maximum radial compression ratio and mean absolute deviation at maximum compression) are given in the last two columns of Table 3. These will be further discussed in the Results Section.

The Results Section is organised as follows: a detailed analysis of experimental data for representative deep cylindrical and shaped implosions (#779 and #777) is presented in Section 4.1. To demonstrate the difference between RT stable and RT unstable interfaces, shot #849 (which is RT unstable) is analysed in Section 4.2. Finally, a comparison between experimental and numerical liner trajectories for the five shots (#779, #777, #897, #898, and #899) is provided in Section 4.3.

4.1. Deep cylindrical and shaped implosion results

4.1.1. Gap pressures

Experimental gap pressures for cylindrical (#779) and shaped (#777) cases in Table 3 are shown in Fig. 5a and 5b, respectively. The full set of accumulator pressures used to produce these gap pressures is presented in Table B1 of Appendix B. Data presented in Fig. 5 were post-processed by applying a 4 kHz low-pass filter to eliminate high-frequency noise while keeping errors in pressure, even for sharp peaks, to less than 1 %. Filtering of the data was required because the pressure transducers (see Section 2.2.1) are sensitive to electromagnetic interference (EMI).

The start time for all diagnostics was synchronised at time zero. The initial gap pressure in both experiments was about 101 kPa. The pressure traces in Fig. 5 exhibit sharp artefacts around $t = 0.041$ s which are caused by EMI from the high-voltage solenoid valve actuation pulse.

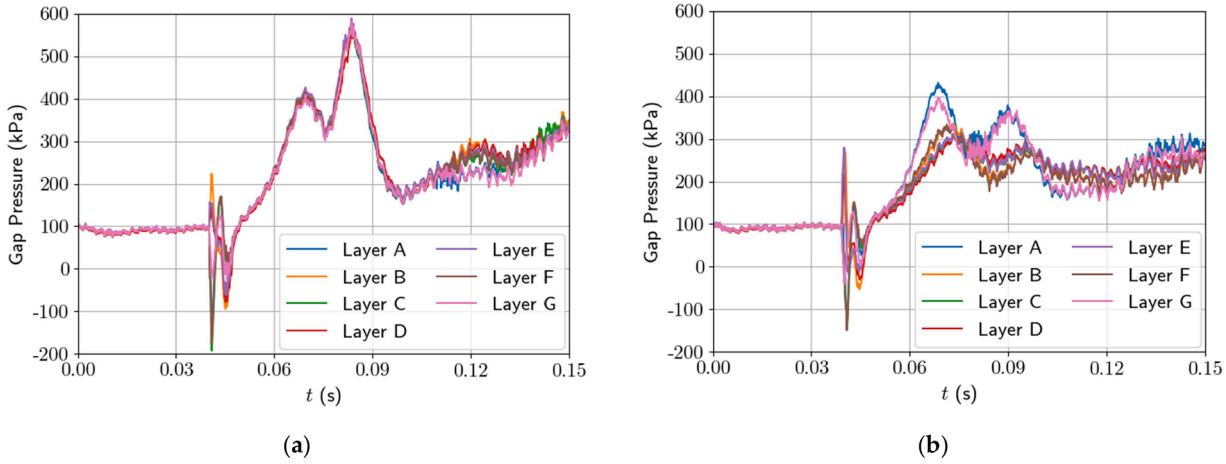

Fig. 5. Experimental gap pressures as a function of time for all horizontal layers. Layers are named A-G from bottom to top (as in Fig. 2). (**a**) a cylindrical implosion (#779, Table 3) and (**b**) a shaped implosion (#777, Table 3). The sharp artefacts around $t = 0.041$ s are electromagnetic interference (EMI) noise from the high-voltage solenoid valve actuation pulse. For similar accumulator pressures and identical valve actuation times, the gap pressures remain nearly identical as in (a). Varying accumulator pressures and valve actuation times results in different gap pressures between layers, as in (b).

This time corresponds to the valves opening and the drive pistons subsequently launching.

As the drive pistons move forward, they compress the gas in front of them (both inside the bore and gap). When the force exerted by gap pressure upon the pusher pistons exceeds a certain threshold, the pusher pistons start to move inwards (launch). This threshold is determined by the centrifugal force due to the rotating liquid and piston, the force due to differential pressure between cavity and gap, and static friction.

The gap pressure increases until its first maximum ($t \approx 0.069$ s), and then starts to decrease as pusher pistons continue to move inwards and the volume occupied by gas inside the pusher bores increases. When the liner attains its minimum radius (maximum compression ratio, also called *turnaround*), gap pressure reaches a local minimum ($t \approx 0.075$ s). Once the liner starts to *rebound (*move outwards following compression), pressure in the gap starts to increase again causing a second peak ($t \approx 0.084$ s). This study is mainly focussed on liner dynamics during the stages of implosion and turnaround.

The general trends in gap pressure data are similar for both cylindrical and shaped implosions. One can see that in the case of the cylindrical implosion (Fig. 5a) gap pressures are very similar for all layers. This is expected, as in this case the accumulator pressures are almost the same and actuation times are identical (see shot #779 in Table 3).

For the shaped implosion, on the other hand, there is a significant difference in the amplitude and shape of the gap pressures between layers, as can be seen in Fig. 5b (see shot #777 in Table 3). This demonstrates that gap pressures can be controlled by varying accumulator pressures and/or valve actuation times, and engaging interlayer seals to minimise pressure equalisation between layers (see Section 2.3.5). In this example, accumulator pressures are highest at the polar layers (A and G), and lower towards the equator (layer D). This manifests in the highest gap pressures being attained at the polar layers, and the lowest at the equator. A time difference ($\Delta t \approx 0.007$ s) in the occurrence of the first gap pressure maxima between polar and equatorial layers is also evident. Finally, it is important to emphasise that it is these variations in gap pressure which provide the impetus to shape the inner surface of the liner.

4.1.2. Piston trajectories

Representative experimental PDV spectrograms for shot #779 for one of the horizontal layers are shown in Fig. 6. The velocities of drive and pusher pistons are presented in parts (a) and (b) respectively. The starting time ($t = 0$) is identical to that in Fig. 5 (see also Section 2.3.4). It can be seen that the drive piston rapidly accelerates after valve opening ($t \approx 0.040$ s), reaching a peak velocity of about 17 m/s at $t \approx 0.057$ s. As gap pressure increases, the drive piston decelerates and bounces back ($t > 0.082$ s). After a number of oscillations, it eventually comes to a stop (oscillations are not shown in Fig. 6a).

The velocity of the pusher pistons, captured by a PDV port in the vessel wall (see Fig. 2e), is shown in Fig. 6b. In this case the velocity trace is discontinuous, because the stationary diagnostic port measures the velocity of each pusher piston as the rotor sweeps past it. The line segments represent velocities of individual pusher pistons within a horizontal layer, while the gaps correspond to sections of the rotor wall between the bores (this alignment is shown in Fig. 2e). Thus, the trace shown is a composite of multiple pusher pistons over the course of the implosion (total of 10 pistons shown in Fig. 6b).

For shot #779 shown in Fig. 6, the pusher piston trace is smooth. This indicates that no collisions of pusher pistons with inner end stops occurred. For shots #777 and #899 (see Table 3), on the other hand, pusher pistons did experience collisions. Collisions can be observed directly in pusher piston PDV data, unless they occur while the PDV port is aligned with the rotor wall. When observed, the velocity data exhibits an abrupt decrease to 0 m/s, often followed by a similarly abrupt increase in velocity in the opposite direction (indicating that the piston bounced back from its inner end stop). It is also worth mentioning that pusher piston collisions may leave a signature in gap pressure signals for their respective layers, wherein a ringing of the signal may be used to infer their occurrence.

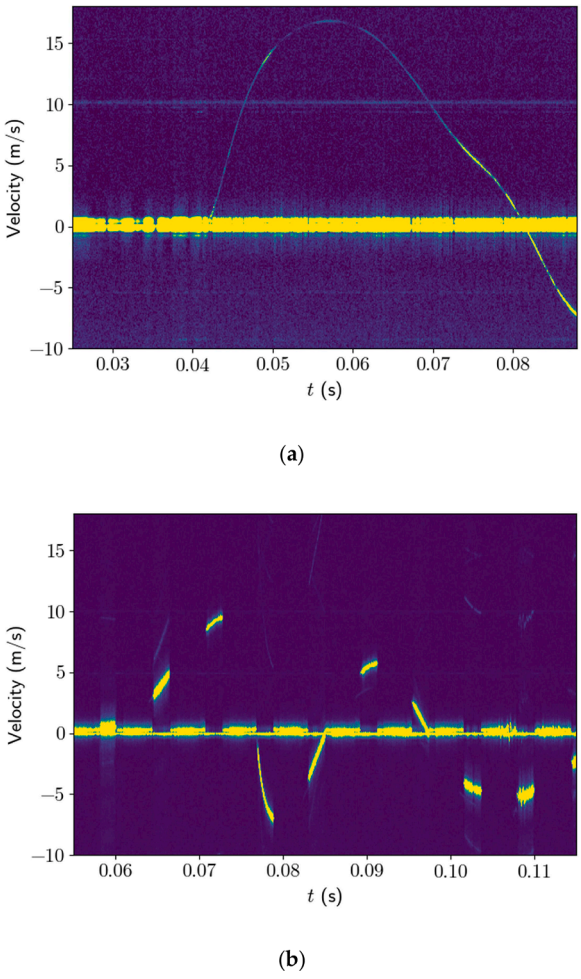

Fig. 6. Representative PDV spectrograms for shot #779 showing the velocity as a function of time for (**a**) a drive piston and (**b**) pusher pistons in a single layer. Note that the launch of the pusher pistons is delayed relative to the drive pistons as it takes time for gas pressure to build up in the gap (approximately 0.060 s). Each line segment represents a different pusher piston in the same layer.

4.1.3. Trajectory and smoothness of the liner surface

In this section the trajectories and smoothness of the liner surface are examined for a cylindrical (#779) and a shaped (#777) implosion. The trajectory of the liner is extracted by tracking reflections of laser planes A, B, C, and D off the surface which are captured by the high-speed camera (see Section 2.3.3). Maintaining a smooth inner surface during the compression phase of Magnetized Target Fusion is important because surface ripples may affect the lifetime of the plasma [6,21,25,46]. To evaluate the smoothness of the surface, data from each laser plane is analysed individually to obtain the radial position of the liner as a function of azimuthal angle, θ. The smoothness dr/r of the liner as a function of time, for a particular axial position z and azimuthal angle θ, is then calculated by Eq. (6):

$$\frac{\mathrm{d}r}{r}(\theta, z, t) = \frac{R(\theta, z, t) - R_{\mathrm{mean}}(z, t)}{R_{\mathrm{mean}}(z, t)}, \tag{6}$$

where $R_{\mathrm{mean}}(z, t)$ is the mean (azimuthally averaged) radius, and $R(\theta, z, t)$ is the radius at any particular position. Thus dr/r represents the deviation of the liner position from the mean at a particular z and θ.

In addition to dr/r, to estimate overall smoothness of the liner at

maximum radial compression, mean absolute deviation was calculated by Eq. (7):

$$Mean\ Absolute\ Deviation(R) = \frac{1}{n}\sum_{i=1}^{n}|R(\theta,\ z,t)\ - R_{\mathrm{mean}}(z,t)| \tag{7}$$

The radial position of the liner as a function of time can be described by the radial compression ratio C_{rad}, defined as:

$$C_{\mathrm{rad}}(z,t) = \frac{R_{\mathrm{mean}}(z,t=0)}{R_{\mathrm{mean}}(z,t)}, \tag{8}$$

where $R_{\mathrm{mean}}(z,t=0)$ is initial mean radius and $R_{\mathrm{mean}}(z,t)$ is mean radius at a particular time t. The highest value of C_{rad} attained at any axial position for any given shot is referred to as the *maximum radial compression ratio* ($C_{rad,\ max}$) in this manuscript.

The volumetric compression ratio C_{vol} as a function of time can also be used to analyse the data, and is calculated as:

$$C_{\mathrm{vol}}(t) = \frac{V(t=0)}{V(t)}, \tag{9}$$

where $V(t=0)$ is initial cavity volume, and $V(t)$ is cavity volume at time t.

Liner trajectories for a deep cylindrical (#779) and shaped (#777) implosion are presented in Figs. 7 and 8, respectively, which follow the same structure. Average trajectories for four laser planes A-D are shown in parts (a), and smoothness of the liner at several instances during the shot is shown in parts (b). In parts (a), the shaded regions represent experimental measurement uncertainty (see Section 2.3.2).

The initial radial position of the liner varies slightly in the axial direction due to gravity. For layer A, the radius is the smallest and it increases toward the equator (layer D), as can be seen in both Figs. 7(a) and 8(a) at $t = 0.060$ s. For the cylindrical implosion in Fig. 7(a), this deviation between layers decreases during the shot, indicating that the liner surface remains nearly cylindrical at all times. The cylindrical shape is expected because the initial accumulator pressures for all layers are almost the same (see Section 2.3.4 and Table 3). The maximum compression ratio is about 7.6, which is at the limit of what is achievable in the CWC. It should be noted that for a compression ratio of 7.6, the liner comes within 0.005 m of the laser plane diagnostic acrylic mounting tube. It is also worth mentioning that for a cylindrical implosion, all layers are visible for most of the shot. This is because higher axial positions (layers C, D) of the liner do not occlude views of the lower ones (layers A, B). However, layers A and B do get occluded deep in compression by the LPD shaft, as previously stated in Section 2.3.3. Finally, the experimental uncertainty (shaded area) is larger at the beginning of the implosion. This is due to fisheye lens distortion becoming higher as the angle from the centre of the camera's field of view increases. The effect of this distortion also becomes more significant at greater radial distances.

For the shaped shot in Fig. 8, the initial radius and shape of the liner are almost identical to that of the cylindrical one. For this shot (#777, see Table 3), the difference between the maximum and minimum accumulator pressures is 1.17 MPa, with the highest pressure of 2.16 MPa used at the top and bottom layers (Layers A, G) and the lowest pressure of 0.99 MPa used at the equator. The trajectories for different layers diverge during the shot, indicating that the liner shape is no longer cylindrical. For this implosion, the maximum radial compression ratio is 7.2:1, which is similar to that of shot #779 (see Fig. 7a) and occurs at the equator. In this case layers A and B are occluded for some portion of the shot due to the shape of the liner, and the equatorial layer is the only one which remains visible throughout the entire shot. The shaded regions, representing experimental uncertainties, are clearly seen in this figure as there is less overlap between trajectories.

Experimental measurements of the smoothness of the liner at several instances (denoted i-v) are presented in Figs. 7(b) and 8(b). These instances were selected to examine smoothness during different phases of the shot: (i) the pre-implosion phase, (ii, iii, iv) around maximum radial

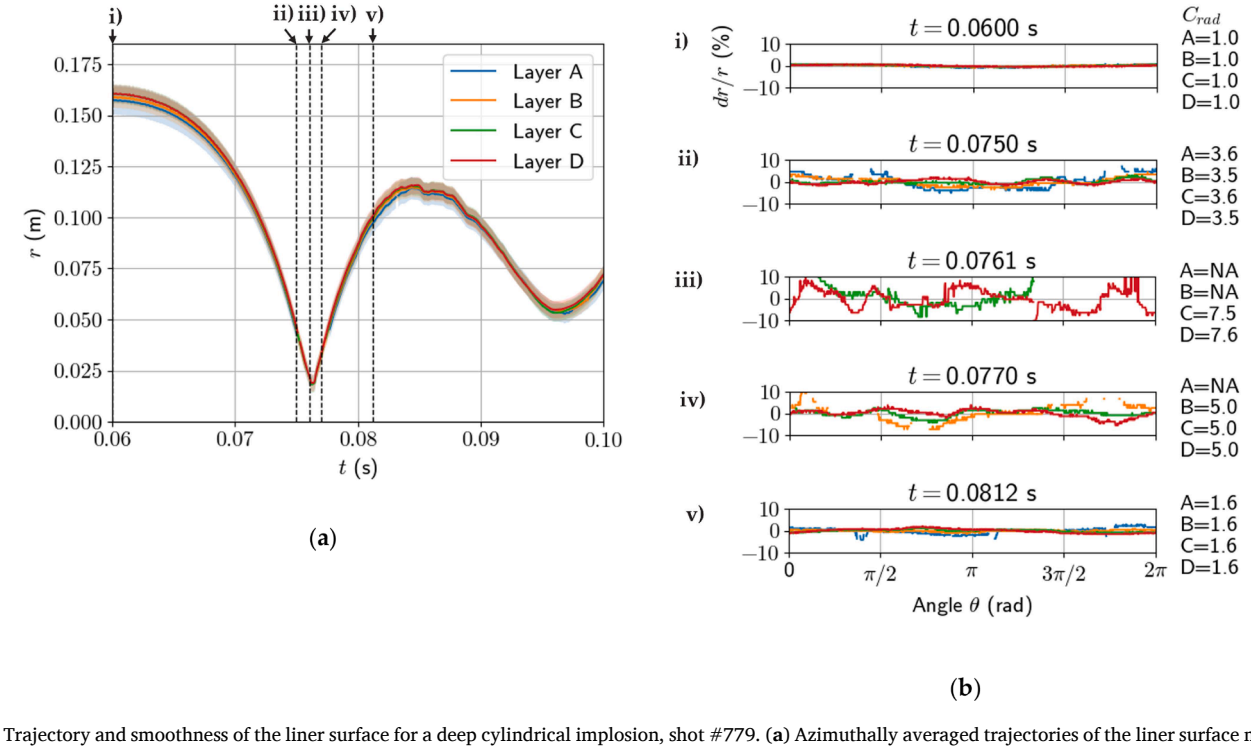

Fig. 7. Trajectory and smoothness of the liner surface for a deep cylindrical implosion, shot #779. (**a**) Azimuthally averaged trajectories of the liner surface measured for laser planes A-D. Shaded regions represent uncertainty of experimental measurements. (**b**) Smoothness, *dr/r*, as function of the azimuthal angle θ at several instances during the shot. Dashed lines marked in part (**a**) as (i)–(v) correspond to the times for which smoothness is shown, where: (i) - pre-implosion; (ii), (iii), and (iv) - in vicinity of turnaround; (v) during rebound. Colour coding of the layers is the same as in part (a). In the vicinity of turnaround some of the planes are occluded by the LPD shaft and data is not available. Radial compression ratio, C_{rad}, attained at different layers is provided on the right-hand side of each figure or marked NA when not available.

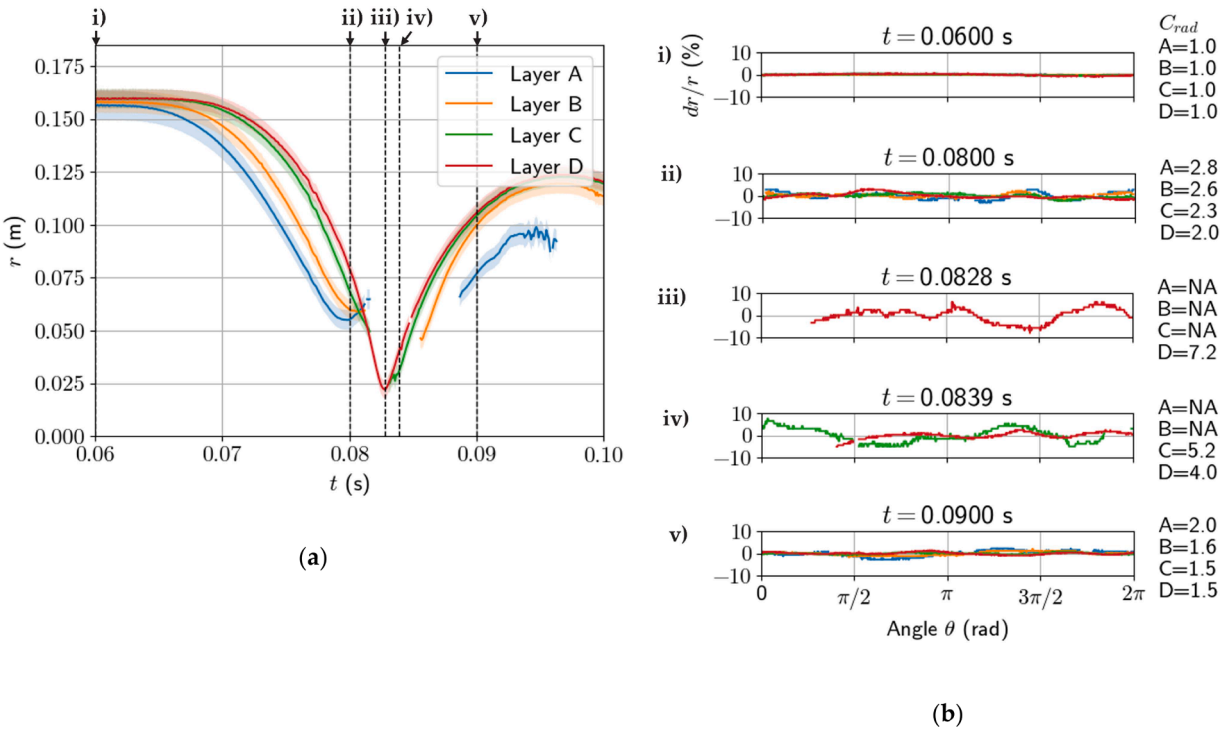

Fig. 8. Trajectory and smoothness of the liner surface for a deep shaped implosion, shot #777. (**a**) Azimuthally averaged trajectories of the liner surface measured for laser planes A-D. Shaded regions represent uncertainty of experimental measurements. (**b**) Smoothness, *dr/r,* as function of the azimuthal angle θ at several instances during the shot. Dashed lines marked in part (a) as (i)–(v) correspond to the times for which smoothness is shown, where: (i) - pre-implosion; (ii)–(iv) - during the implosion phase; (v) during rebound. Colour coding of the layers is the same as in part (a). Some planes are occluded during the shot and data is not available. Radial compression ratio, C_{rad}, attained at different layers is provided on the right-hand side of each figure or marked NA when not available.

compression, and (v) during rebound. The radial compression ratio, C_{rad}, attained by each layer is also provided for instances shown in the figure. If data is not available, it is denoted by NA.

It can be seen from the figures that trends in smoothness evolution are similar for both cylindrical and shaped implosions. The liner surface is initially smooth with *dr/r* below ±1 %. *dr/r* then increases during the implosion phase and reaches its maximum in the vicinity of the turnaround point but remains within ±10 % at all times. It is interesting to note that around peak compression, some low azimuthal mode number perturbations have developed. As the liner rebounds, the surface perturbations diminish again.

At maximal radial compression ratio, the overall smoothness of the inner surface of the liner was also characterised by calculating as the mean absolute deviation (Eq. (7)). In general, the mean absolute deviation increases with compression ratio, and remains within 0.0011 m for all shots, as can be seen in Table 3. It may also be noted that the mean absolute deviation appears to decrease with increasing rotation rate.

4.2. Rayleigh-Taylor unstable implosion

The objective of this section is to demonstrate that by analysing laser reflection patterns, it is possible to distinguish between well-defined (Rayleigh-Taylor stable) and foamy (Rayleigh-Taylor unstable) air-water interfaces during the shot. As a reminder, Rayleigh-Taylor (RT) instability is an instability of an interface between two fluids of different densities which occurs when the lighter fluid is accelerated into the heavier fluid [33,47]. In this case, the net acceleration is directed from the lighter towards the heavier fluid [48]. In this work this happens when the imploding liquid liner is decelerated by the pressurised gas inside the cavity. For a rotating liner, RT instability can be suppressed if the sum of centripetal and radial accelerations at the interface is negative [23–26].

As was mentioned earlier, the parameters for all but the last shot in Table 3 (#849) were chosen such that inner surface of the liner remains Rayleigh-Taylor stable during the entire shot (implosion, turnaround and rebound phases). For those shots, the pattern of the laser reflections indicated that the air-water interface remained well defined (*e.g.,* Fig. 3b), which made it possible to extract surface trajectory and smoothness accurately.

To illustrate the difference between RT stable and RT unstable interfaces, parameters for shot #849 were chosen in such a way that initial rotation of the liner was not sufficient to suppress Rayleigh-Taylor instability during the entire shot (for the accumulator pressures and initial cavity pressure set in the experiment). Development of the Rayleigh-Taylor instability at the liner surface was also confirmed by numerical simulation carried out for the parameters of shot #849. Guided by the results of this simulation, two instances for which the interface is expected to be well-defined (RT stable) and foamy (RT unstable) were selected from the experimental video and are shown in Fig. 9(a) and Fig. 9(b), respectively. The frame shown in Fig. 9(a) corresponds to an instant during the implosion phase and that in Fig. 9(b) is after turnaround. One can see that the laser reflection pattern is significantly different, making it possible to identify whether the inner surface is RT stable or not. The liner trajectory and smoothness analysis for this shot is presented in Supplementary Material Section S3.

It is worth noting that despite achieving complete suppression of RT instability for the shaped implosions in the CWC, this result may only apply to cases where the flow is primarily in a cylindrically radial direction and the axial velocity component is small. In this work, the shaping of the inner surface of the liner was achieved mainly by varying velocities between cylindrical layers. As such, the centripetal and radial acceleration vectors are collinear. However, this would not be the case for a true spherical implosion, where the angle between the radial (in spherical coordinates) and centripetal acceleration vectors increases toward the poles.

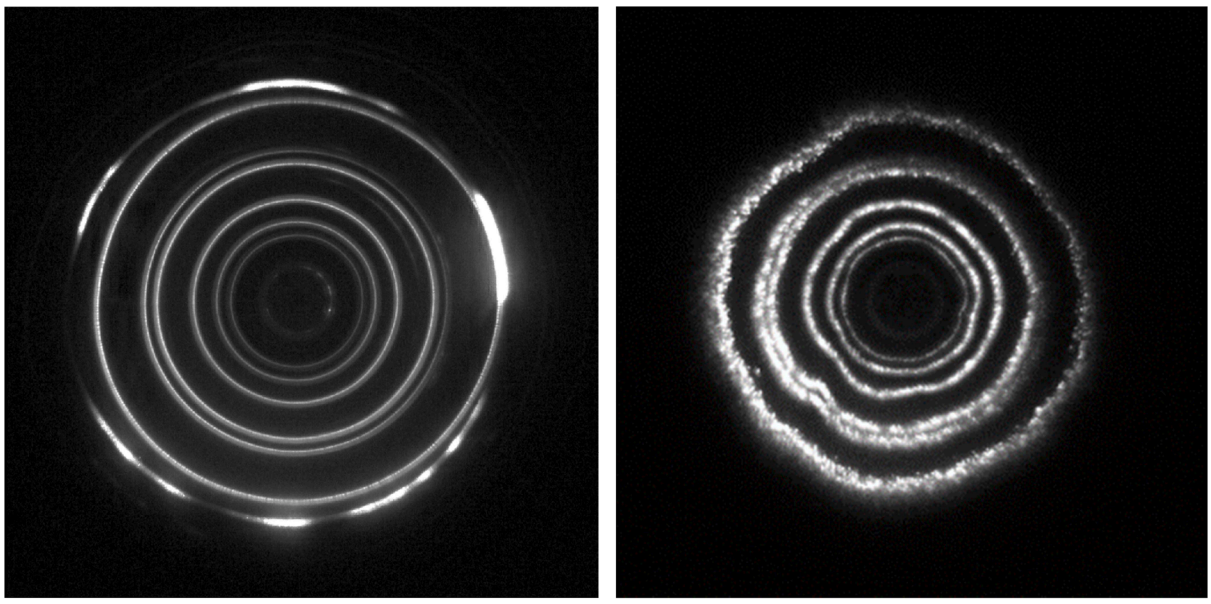

(**a**) (**b**)

Fig. 9. High speed video frames showing laser reflections at two different instances of shot #849. (**a**) early stage of the implosion; interface is predicted to be RT stable; (**b**) after turnaround; interface is predicted to be RT unstable. Well-defined and foamy interfaces can easily be distinguished by looking at the laser reflection patterns.

4.3. Trajectory evolution comparison

Comparison between liner trajectories obtained in experiments and numerical simulations for the first five shots in Table 3 is presented in Figs. 10–14. The radial position of the liner surface is extracted at several axial locations corresponding to the laser planes A, B, C, D, D15 (if available), and cone (if available). Figs. 10–14 have the same structure and consist of the following parts: (a) data for Layer A (bottom layer) shown by the blue lines; (b) data for Layer B shown by the orange lines; (c) data for layer C shown by the green lines; (d) data for Layer D (at equator) shown by the red lines; (e) data for Layer D15 (15 mm above equator) shown by the purple lines (if available) and (f) data for cone shown by the brown lines (if available). Experimental trajectories are plotted as solid lines and those obtained in numerical simulations with OpenFOAM are shown by dashed lines. The shaded area around the solid lines indicates uncertainty of the experimental measurements. The location of the outer surface of the diagnostic shaft is shown by the horizontal dashed line to emphasise the compression depth during the implosion. Gap pressures and rotor speed time histories (experimentally measured and pre-processed versions used in simulations) for each of the shots presented in Figs. 10–14 are provided in Appendix A (Figs. A1–A5). It is worth reiterating that numerical modelling was mainly aimed at predicting liner trajectory during implosion and turnaround, and, therefore, no attempt was made to simulate liner dynamics for longer times.

Trajectories for a deep cylindrical implosion (shot #779) are shown in Fig. 10. One can see that for a cylindrical implosion there is excellent agreement between experimental and numerical data. The maximum radial compression attained in this shot is at the limit of what is possible with the CWC, as the liner surface is almost touching the diagnostic shaft at the liner turnaround point.

Trajectories for two shaped implosions, shots #897 and #898, are shown in Fig. 11 and Fig. 12, respectively. For these shots data are available for all laser planes as well as the cone. Accumulator pressures are highest for the top and bottom layers (A and G) and lowest at the equator (layer D). The maximum difference in accumulator pressures, which is related to the extent of shaping, is 0.59 MPa in shot #897 and 0.72 MPa in shot #898 (see Table 3). Initial rotor speed for these shots is identical and is higher than for the deep implosion shots (#779 and #777) by about 7.5 %. The initial cavity pressure is similar to that in shot #779 (about 1.5 % difference). Increasing the initial rotor speed results in a decrease of the maximum radial compression ratio attained in those shots. Agreement between the experimental and numerical trajectories is very good for both shaped implosions.

Trajectories for two additional shaped implosions (#899 and #777) are presented in Fig. 13 and Fig. 14, respectively. In these shots the maximum difference in accumulator pressures between the layers was higher than in the shaped shots #897 and #898. For #899 it was about 0.83 MPa, and for the deep shaped shot #777 it was about 1.16 MPa (see Table 3). For shot #899 both initial rotor speed and accumulator pressures were lower than for #897 and #898, while the attained maximum radial compression ratio is very similar. For the deep shaped implosion, shot #777, the initial rotor speed was the same as for the deep cylindrical implosion, shot #779, and accumulator pressures for the top and bottom layers were the highest of all the shots presented. The greater variation in accumulator pressures between layers was intended to achieve more pronounced shaping of the liner. The unintentional consequence was that pusher pistons in some layers hit their inner end stops during the implosion (see Table 3). The hardest collisions happened during the deep shaped shot #777, for the top and bottom layers (A and G). Collisions were also detected for top and bottom layers in shot #899, but to a lesser extent. From the moment collisions occur, gap pressure acting on the pusher pistons is no longer felt by the liner. The expected trajectory of the liner is changed, and the most pronounced inconsistency can be seen in trajectories for layers A and B for shot #777 (Fig. 14a and 14b).

The current numerical model does not capture this scenario, and, therefore, cannot be used to predict the liner trajectory after pusher piston collisions. It can, however, confirm the possibility of collisions by following the position of the inner edge of the additional liquid representing the pusher pistons. If this edge passes the exit of the bore on its way inward, then collisions between pusher pistons and their inner end stops are likely to occur in the experiment. For both shaped shots #899 (Fig. 13) and #777 (Fig. 14) this was found to be the case and is in agreement with the analysis of the experimental data (see Section 4.1.2). Therefore, for these shots, numerical data are provided only until the

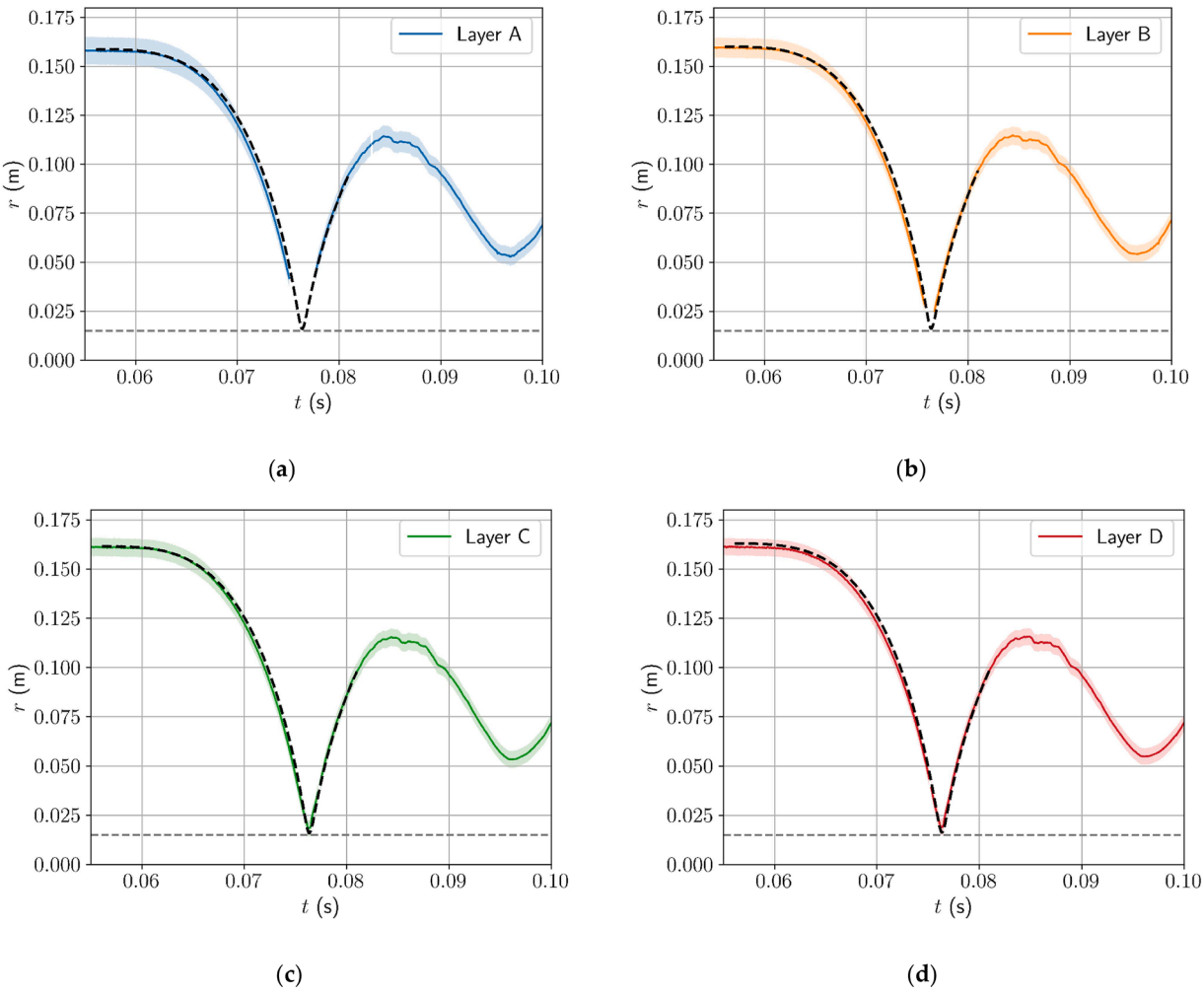

Fig. 10. Trajectories of the inner surface of the liner for a deep cylindrical implosion, shot #779 in Table 3. Experimental and numerical (OpenFOAM) data are shown by solid (coloured) and dashed (black) lines, respectively. Parts (**a**)–(**d**) correspond to the inner surface trajectories at the axial positions of the laser planes A-D (see Figs. 3a and 4a). Shaded areas indicate the range of experimental uncertainty. The position of the outer surface of the diagnostic shaft is shown by the horizontal dashed line. Shot parameters: $\Omega_0 = 50.3$ rad/s, $p_{\text{accumulator}} = 1.98$-$1.99$ MPa, $p_{\text{cavity}} = 5.38$ kPa.

moment of the first collision, as beyond this point the model is no longer valid. Until then, the numerical data agree very well with experimental measurement for both shots.

The shape evolution of the liner surface presented in Figs. 10–14 is plotted in a different format in Fig. 15. Each part of the figure corresponds to a particular shaped implosion in Table 3; (a) #897, (b) #898, (c) #899, and (d) #777. In Fig. 15, the radial position of the inner surface of the liner as a function of the axial position, z, is shown for several volumetric compression ratios (see Eq. (6)) during early stages of implosion, when experimental data are available for all layers. Simulation profiles are shown by the dashed black lines, while dots correspond to the experimental measurements for layers A to D. Short horizontal lines across the dots indicate the range of experimental uncertainty. The profiles are shown only for the lower half of the rotor (from the bottom to the equator), where the LPD operates. For all shots there is excellent agreement between experimental and numerical profiles, further confirming that the simplified numerical model is capable of predicting the evolution of the liner surface accurately.

With respect to the shaping of the liner surface, the following observations can be made: (i) a nearly cylindrical initial liner surface is shaped during the shot when accumulator pressures (and solenoid valve opening times for shot #777) are varied between the layers. In all shots presented in Fig. 15, accumulator pressures are highest at the bottom (and top) layers and lowest at the equator. This results in liquid near the bottom and top initially moving faster than that at the equator. (ii) Differences in the radial position of the liner surface in the axial direction correlate with differences in accumulator pressures. More pronounced shaping is achieved for shots #899 (Fig. 15c) and #777 (Fig. 15d) for which accumulator pressure differences between layers are larger than for shots #897 (Fig. 15a) and #898 (Fig. 15b).

5. Conclusions

A 1/10th scale version of the FDP plasma compression system, called the CWC, was constructed at General Fusion to de-risk the liner implosion scheme. This paper summarises experimental results obtained with the CWC and their comparison to simplified numerical modelling. The size of the CWC and its performance goals were defined with the intention of reaching a sufficiently challenging operating regime to identify potential issues we could encounter enroute to the FDP, whilst keeping the machine cost within budget. As such, requirements for shaping the liner, the maximum compression ratio, and the smoothness of the liner are expected to be more aggressive on the FDP.

From the conceptual point of view, the two major achievements of this work are: (i) experimental demonstration of high compression implosions with a high degree of symmetry by imploding the liner with arrays of discrete pneumatic pistons, and (ii) experimental demonstration of shape manipulation of the inner surface of the liner during

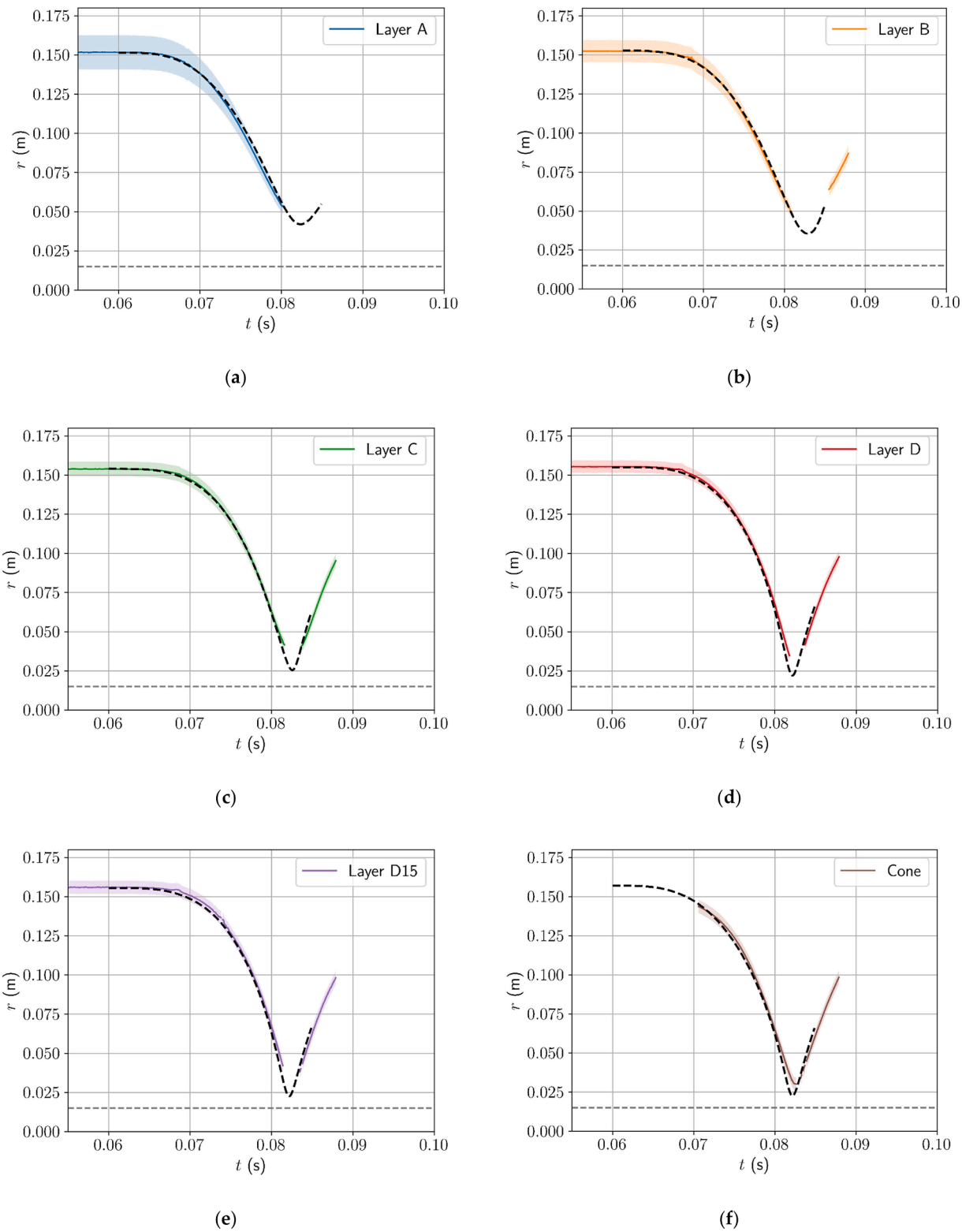

Fig. 11. Trajectories of the inner surface of the liner for a shaped implosion, shot #897 in Table 3. Experimental and numerical (OpenFOAM) data are shown by solid (coloured) and dashed (black) lines, respectively. Parts (**a**)–(**f**) correspond to the inner surface trajectories obtained at axial positions of the laser planes A-D15 and cone (see Figs. 3a and 4a). Shaded areas indicate the range of experimental uncertainty. The position of the outer surface of the diagnostic shaft is shown by the horizontal dashed line. Shot parameters: $\Omega_0 = 57.1$ rad/s, $p_{\text{accumulator}} = 1.22\text{-}1.81$ MPa, $p_{\text{cavity}} = 5.45$ kPa.

implosions by adjusting accumulator pressures and solenoid valve opening times between horizontal layers. The former is very important because it confirms that despite having discrete pneumatic pistons pushing on the liner, it is feasible for the inner surface of the liner to remain sufficiently smooth for high compression ratio implosions. The latter means that it is feasible to start with a cylindrical liner rotating as a solid body and shape its inner surface toward a spherical one as it implodes. This avoids the challenges of forming an initially spherical,

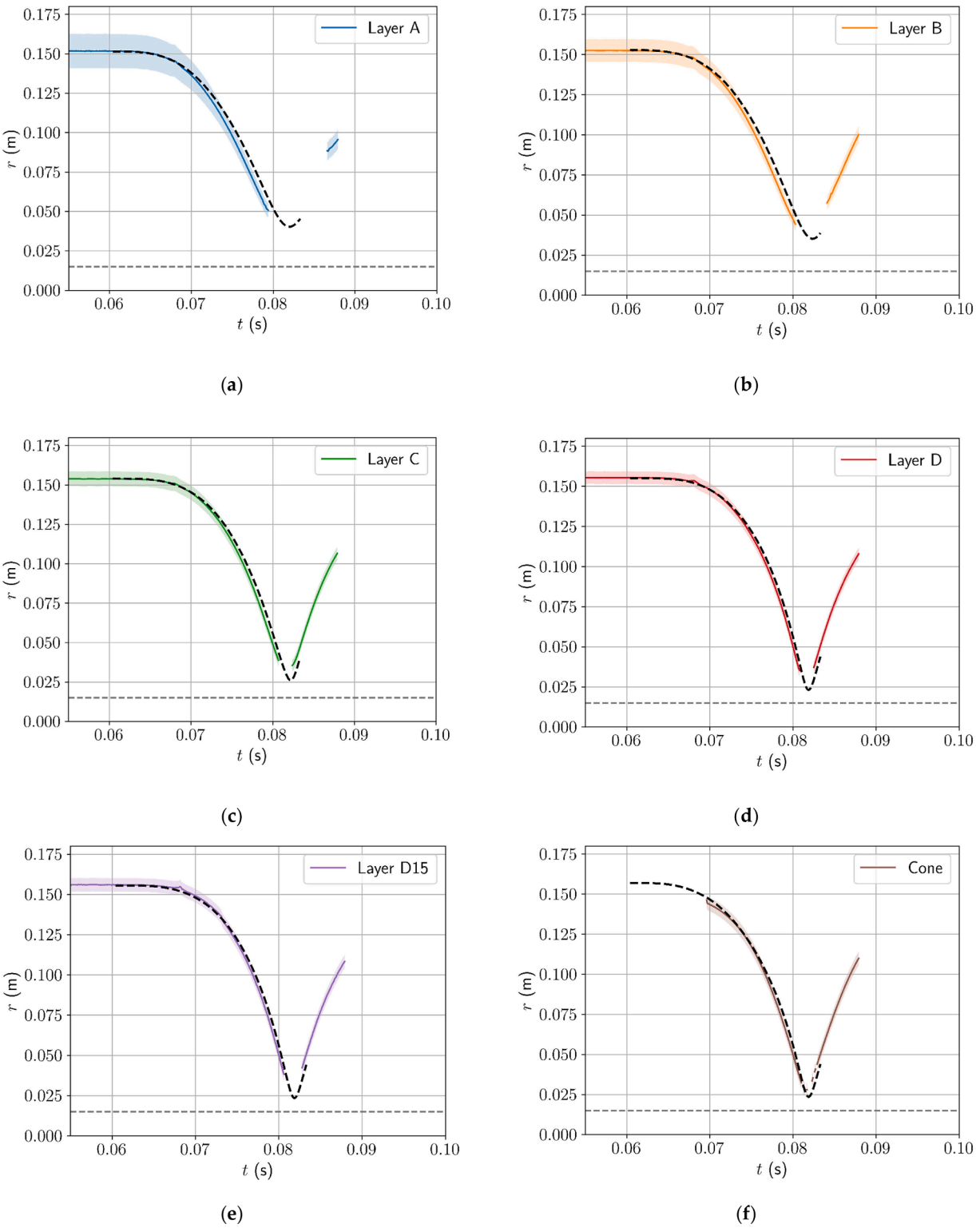

Fig. 12. Trajectories of the inner surface of the liner for a shaped implosion, shot #898 in Table 3. Experimental and numerical (OpenFOAM) data are shown by solid (coloured) and dashed (black) lines, respectively. Parts (**a**)–(**f**) correspond to the inner surface trajectories obtained at axial positions of the laser planes A-D15 and cone (see Figs. 3a and 4a). Shaded areas indicate the range of experimental uncertainty. The position of the outer surface of the diagnostic shaft is shown by the horizontal dashed line. Shot parameters: $\Omega_0 = 57.1$ rad/s, $p_{\text{accumulator}} = 1.19\text{-}1.91$ MPa, $p_{\text{cavity}} = 5.45$ kPa.

rotating liquid cavity with a smooth inner surface [49].

It was also experimentally demonstrated that Rayleigh-Taylor instability can be completely suppressed by sufficient rotation for shaped implosions, at least when liner flow is predominantly in a cylindrically radial direction. This is a new result, and to the best of our knowledge, studies of rotational suppression of RT instability have been limited to purely cylindrical implosions. However, extrapolation of this result to different implosion schemes must be done with caution. The outcome will depend on the time history of the axial acceleration component, because there is no rotational stabilisation mechanism in

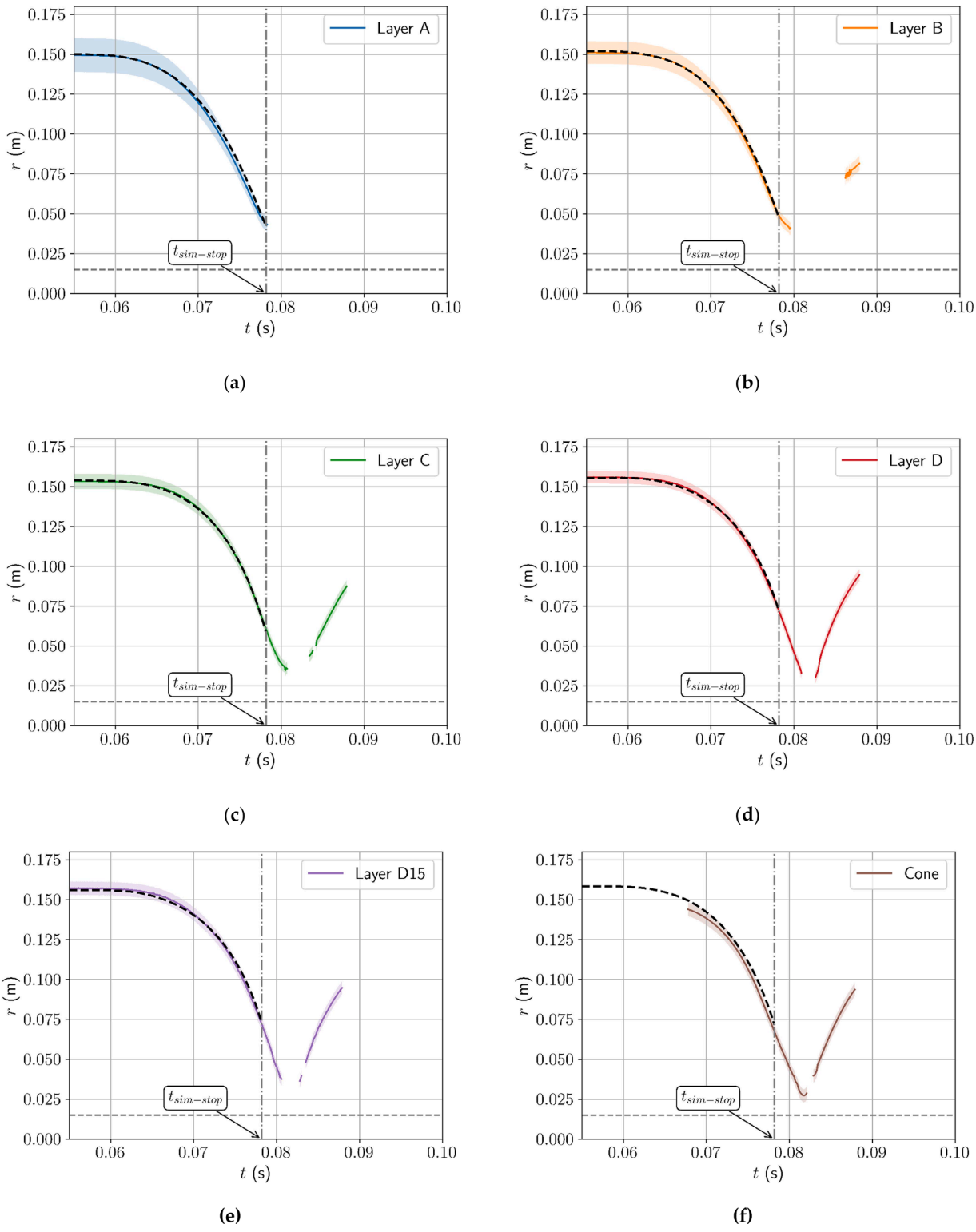

Fig. 13. Trajectories of the inner surface of the liner for a shaped implosion, shot #899 in Table 3. Experimental and numerical (OpenFOAM) data are shown by solid (coloured) and dashed (black) lines, respectively. Parts (**a**)–(**f**) correspond to the inner surface trajectories obtained at axial positions of the laser planes A-D15 and cone (see Figs. 3a and 4a). Shaded areas indicate the range of experimental uncertainty. The position of the outer surface of the diagnostic shaft is shown by the horizontal dashed line. The vertical dash-dot line corresponds to the earliest time when the inner surface of the additional liquid (representing the pusher pistons) reaches the inner end of a pusher bore in the simulation, indicating a collision. Numerical data were truncated at this time as the numerical model is no longer valid. Shot parameters: $\Omega_0 = 45.0$ rad/s, $p_{\text{accumulator}} = 0.89\text{-}1.72$ MPa, $p_{\text{cavity}} = 8.00$ kPa.

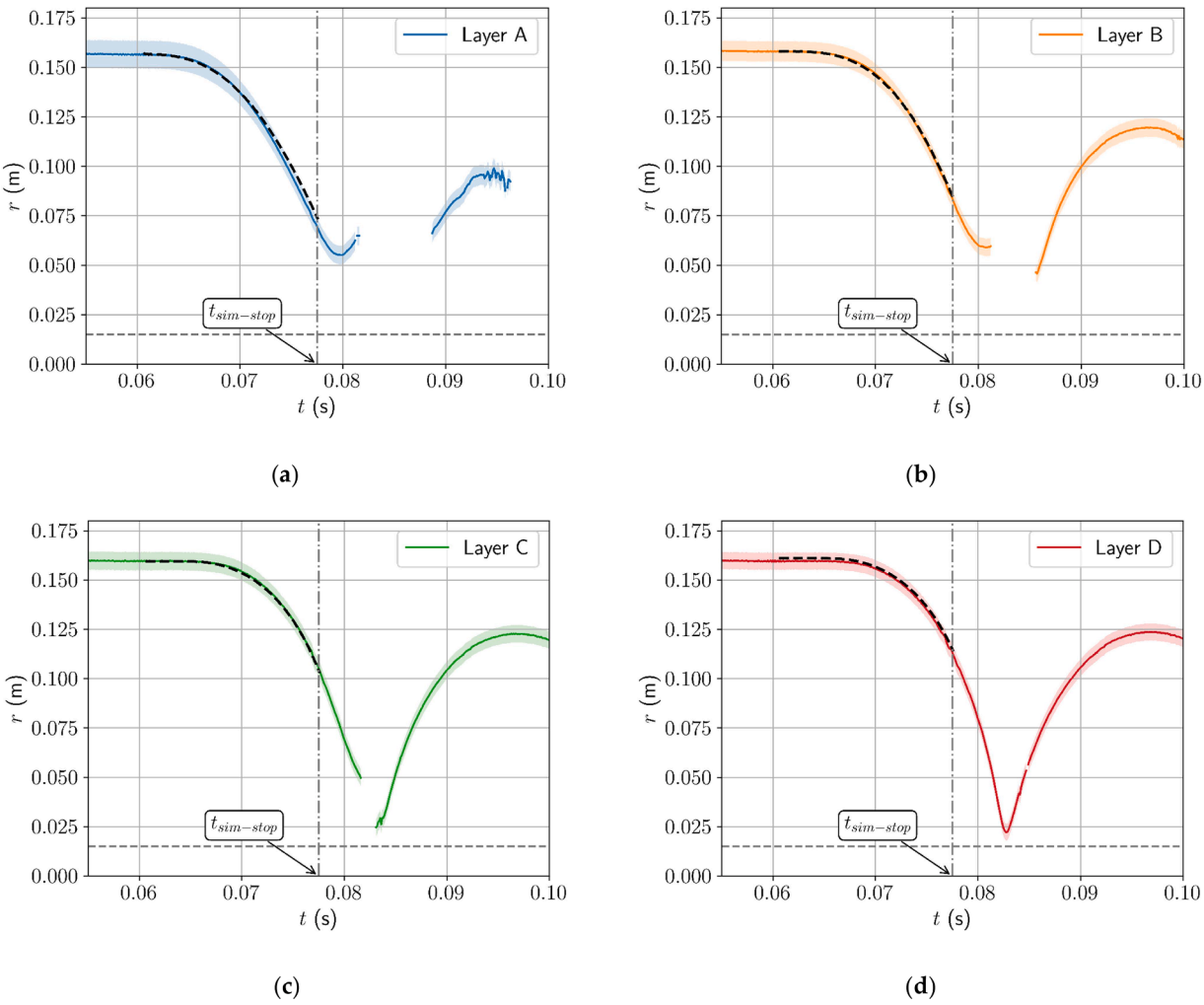

Fig. 14. Trajectories of the inner surface of the liner for a deep shaped implosion, shot #777 in Table 3. Experimental and numerical (OpenFOAM) data are shown by solid (coloured) and dashed (black) lines, respectively. Parts (**a**)–(**d**) correspond to the inner surface trajectories at the axial positions of the laser planes A-D (see Figs. 3a and 4a). Shaded areas indicate the range of experimental uncertainty. The position of the outer surface of the diagnostic shaft is shown by the horizontal dashed line. The vertical dash-dot line corresponds to the earliest time when the inner surface of the additional liquid (representing the pusher pistons) reaches the inner end of a pusher bore in the simulation, indicating a collision. Numerical data were truncated at this time as the numerical model is no longer valid. Shot parameters: $\Omega_0 = 50.3$ rad/s, $p_{\text{accumulator}} = 0.99$-$2.16$ MPa, $p_{\text{cavity}} = 5.45$ kPa.

this direction.

To date, RT stable implosions with maximum radial compression ratios up to 7.6:1 were achieved with the CWC. Smoothness of the liner, *dr/r*, remained under 10 % at all times and mean absolute deviation at maximum radial compression was 1 mm or less for the shots considered. A general trend is that values of *dr/r* and mean absolute deviation at maximum compression increase with increasing compression ratio, which is expected. It is worth keeping in mind that the maximum radial compression ratio which can theoretically be achieved in the CWC with its current diagnostic shaft is 10:1. Relative to the diagnostic shaft (LPD), the compression ratio is higher yet. For example, if the compression ratio is defined as $(r_0\text{-}R_{\text{shaft}}) / (r\text{-}R_{\text{shaft}})$, then the radial compression ratio for the 7.6:1 shot becomes ~ 20:1.

A simplified model to simulate the rotating part of the apparatus was developed using OpenFOAM open-source software. Key simplifications were reducing the dimensionality of the problem from 3D to 2D axisymmetric, eliminating moving parts by representing solid pistons as additional liquid, assuming laminar liner flow, and omitting small-scale geometrical features. Very good agreement between numerical modelling and experimental measurements was observed for a wide range of shot parameters. The simplified model can now be used as a predictive tool for designing MTF machines with more confidence.

The LPD system was developed to measure the trajectory of the liner in the CWC and was found to function reliably under a wide range of conditions. The PDV system used to measure the velocity of pusher pistons in the rotor from a stationary diagnostic port on the vessel was also effective, but a greater number of channels would be required to obtain more complete data. A pressure sensor mounted inside the cavity of the CWC would provide another means of comparing experimental data to simulations.

As General Fusion moves toward a full-scale prototype operating with liquid metal (FDP), future studies will include: (i) exploring the effect of rotor geometry (bore size and number of horizontal layers), (ii) structural integrity of the rotor as machine size increases, (iii) understanding of the dynamic response of the rotor and vessel during liner implosion, (iv) exploring liner dynamics for longer times, until a smooth liner surface is re-established, (v) achieving higher maximum compression ratios with required level of surface smoothness, (vi) achieving an optimised shape of the inner surface of the liner within engineering constraints, and (vii) development of liner diagnostics which are compatible with conditions within the FDP. The CWC and its future modifications will allow us to make progress in the areas above.

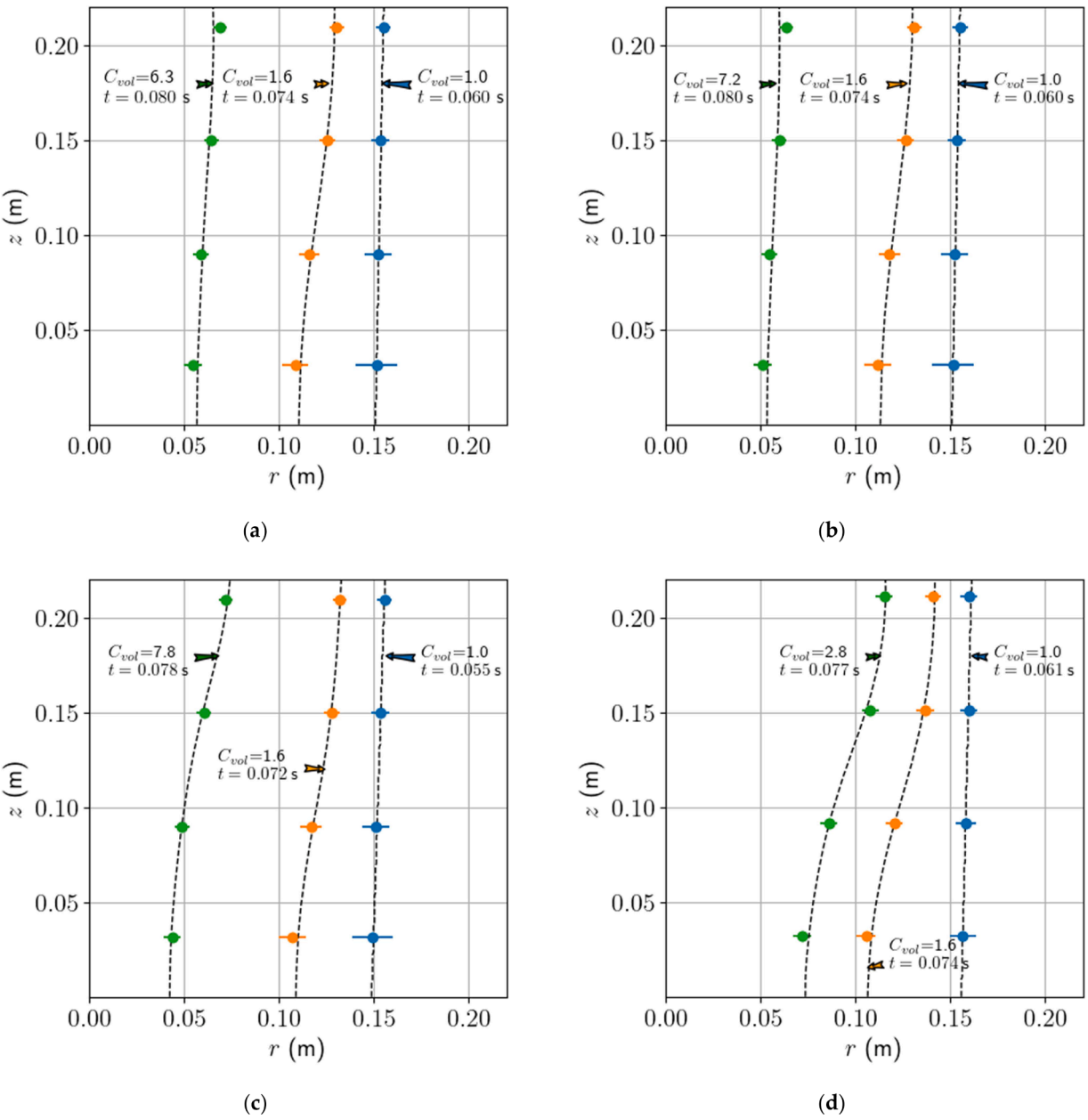

Fig. 15. The shape of the inner surface of the liner obtained in experiments and numerical simulations shown for several volumetric compression ratios (C_{vol}) (Eq. (6)) during the early stages of the implosion. Numerical profiles are shown by the black dashed lines and experimental data are shown by the coloured dots. Colours correspond to a particular volumetric compression ratio. Short horizontal lines across the dots indicate the range of experimental uncertainty. (a) shot #897, (b) shot #898, (c) shot #899, (d) shot #777. The corresponding times at which these C_{vol} values were attained are also shown.

Funding

This research did not receive any specific grant from funding agencies in the public, commercial, or not-for-profit sectors.

CRediT authorship contribution statement

Nicholas S. Mangione: Methodology, Formal analysis, Writing – original draft, Writing – review & editing. **Hao Wu:** Validation, Formal analysis, Writing – original draft, Visualization. **Claire Preston:** Software, Formal analysis, Writing – original draft, Visualization. **Anthony M.D. Lee:** Formal analysis, Writing – review & editing, Visualization. **Sohrab Entezami:** Software, Formal analysis, Writing – original draft, Visualization. **Raphaël Ségas:** Software, Validation, Formal analysis, Visualization, Writing – review & editing. **Piotr W. Forysinski:** Conceptualization, Methodology, Writing – review & editing, Project administration. **Victoria Suponitsky:** Conceptualization, Methodology, Writing – original draft, Writing – review & editing, Project administration.

Declaration of Competing Interest

The authors declare that they have no known competing financial interests or personal relationships that could have appeared to influence the work reported in this paper.

Data availability

Data will be made available on request.

Acknowledgments

The authors would like to acknowledge the entire General Fusion team for making this work possible. The authors also thank Prof. Andrew Higgins for his insightful comments on the manuscript.

Supplementary materials

Supplementary material associated with this article can be found, in the online version, at doi:10.1016/j.fusengdes.2023.114087.

Video S1: Shot #779 Cylindrical Video Montage, Video S2: Shot #777 Shaped Video Montage, Video S3: Shot #897 Shaped Video Montage, Video S4: Shot #898 Shaped Video Montage, Video S5: Shot #899 Shaped Video Montage, Video S6: Shot #849 RT Unstable Video Montage.

Appendix A

Gap pressures and rotor speed data for the five shots in Table 3 (#779, #897, #898, #899, and #777) are provided in Figs. A1–A5. All figures follow the same structure and consist of the following parts: (a) experimental gap pressures for horizontal layers A-G; (b) experimental rotor speed data (raw data are shown by the blue dotted line and filtered data are shown by the black dashed line); (c) pre-processed gap pressures for horizontal layers A-G used in numerical simulations; (d) pre-processed rotor speed used in numerical simulations. The shaded areas in parts (a) and (b) of the figures indicate the range of experimental data used in simulations. The start of the shaded area ($t = 0$ in simulation) aligns with the start of the liner's inward motion, which correlates with the increase in rotor speed as shown in parts (b). If simulations were run longer into the rebound phase, a constant pressure corresponding to the value at which the pressure signal was truncated was used for the rest of the simulation. Experimental data were smoothed using a 4 kHz low-pass filter for pressure, and a linear regression over each ten-element window for rotor speed, before being applied in simulations.

A challenge encountered in using experimental gap pressure data as input for simulations is determining the starting point for liner motion. As there is nothing in the current simulation setup to prevent outward movement of the liner, the applied gap pressure should be equal to or higher than centrifugal pressure due to liner rotation. In the CWC the end stop at the outer end of the pusher piston bore covers about 30 % of the bore cross-sectional area. Because of this, the gap pressure required to move the liner should be a factor of 1.3 higher than centrifugal pressure, if friction is insignificant, and if it is assumed that the pusher piston seals against the end stop. Friction appeared to be negligible for all shots except #777 (see introduction to Section 4). The initial segment of experimental data when the pressure is lower than 1.3 times the centrifugal pressure was not used in simulations. For #777 the threshold was increased to 1.8 times the centrifugal pressure, because static friction for this shot was considerably higher compared to others as it was the first shot in the series. For shaped implosions, the pressure threshold is reached at different times for different layers, as accumulator pressures vary between layers. In this case, before the threshold value is reached, the signal was replaced by centrifugal pressure.

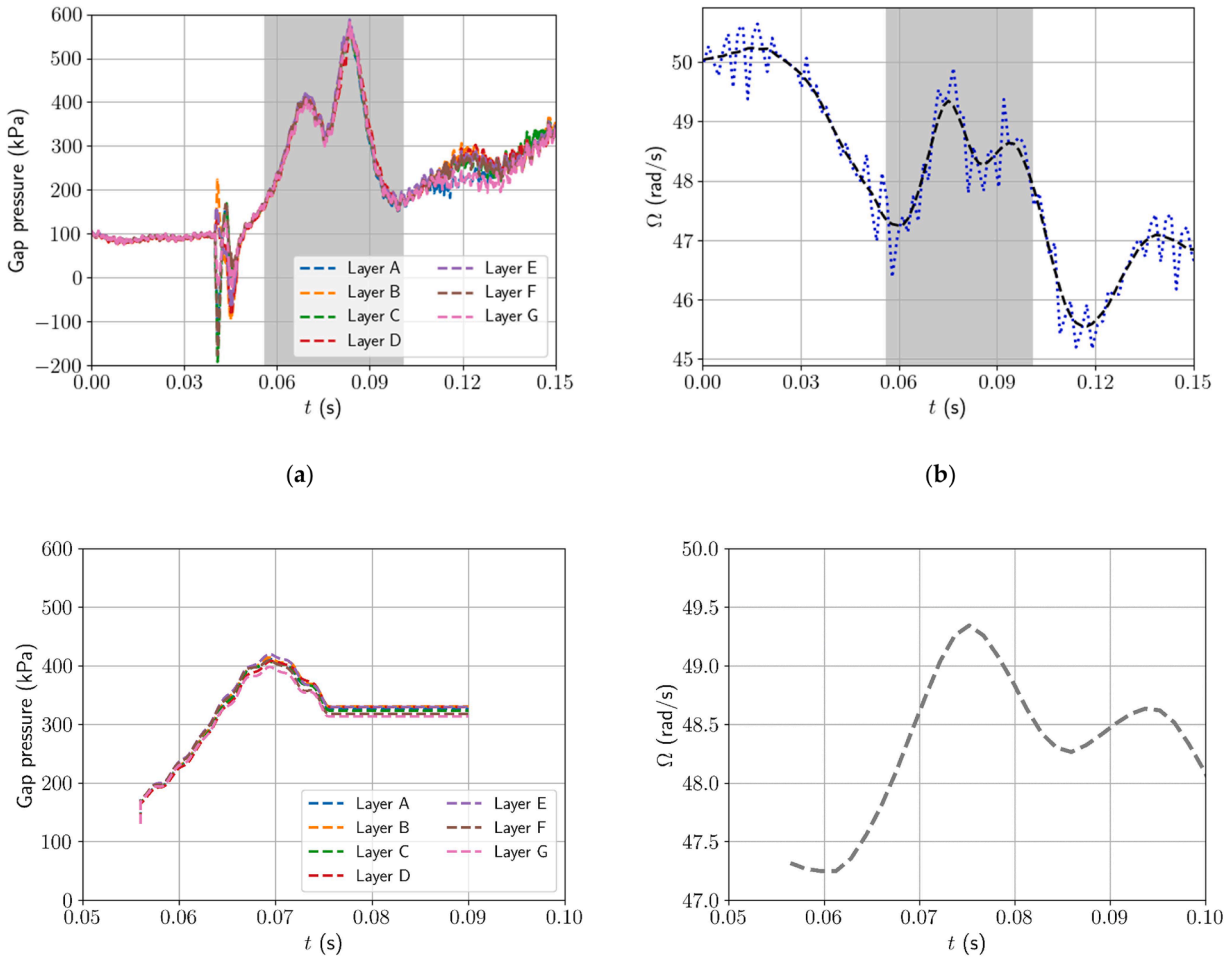

Fig. A1. Gap pressure and rotor speed data for a deep cylindrical implosion, shot #779 in Table 3. (**a**) Filtered gap pressure signal (Section 4.1.1) measured in the experiment. (**b**) Rotor speed measured in the experiment. Blue dotted line – raw signal, black dashed line - filtered signal. (**c**) Gap pressure data used as input into simulation. (**d**) Rotor speed data used as input into simulation. Shaded regions in (a) and (b) indicate time range of experimental data used as inputs into simulation. The fluctuation in rotor speed in the experiments is due to the friction (inter-layer seals) and change of the amount of liquid inside the pusher bores during the shot.

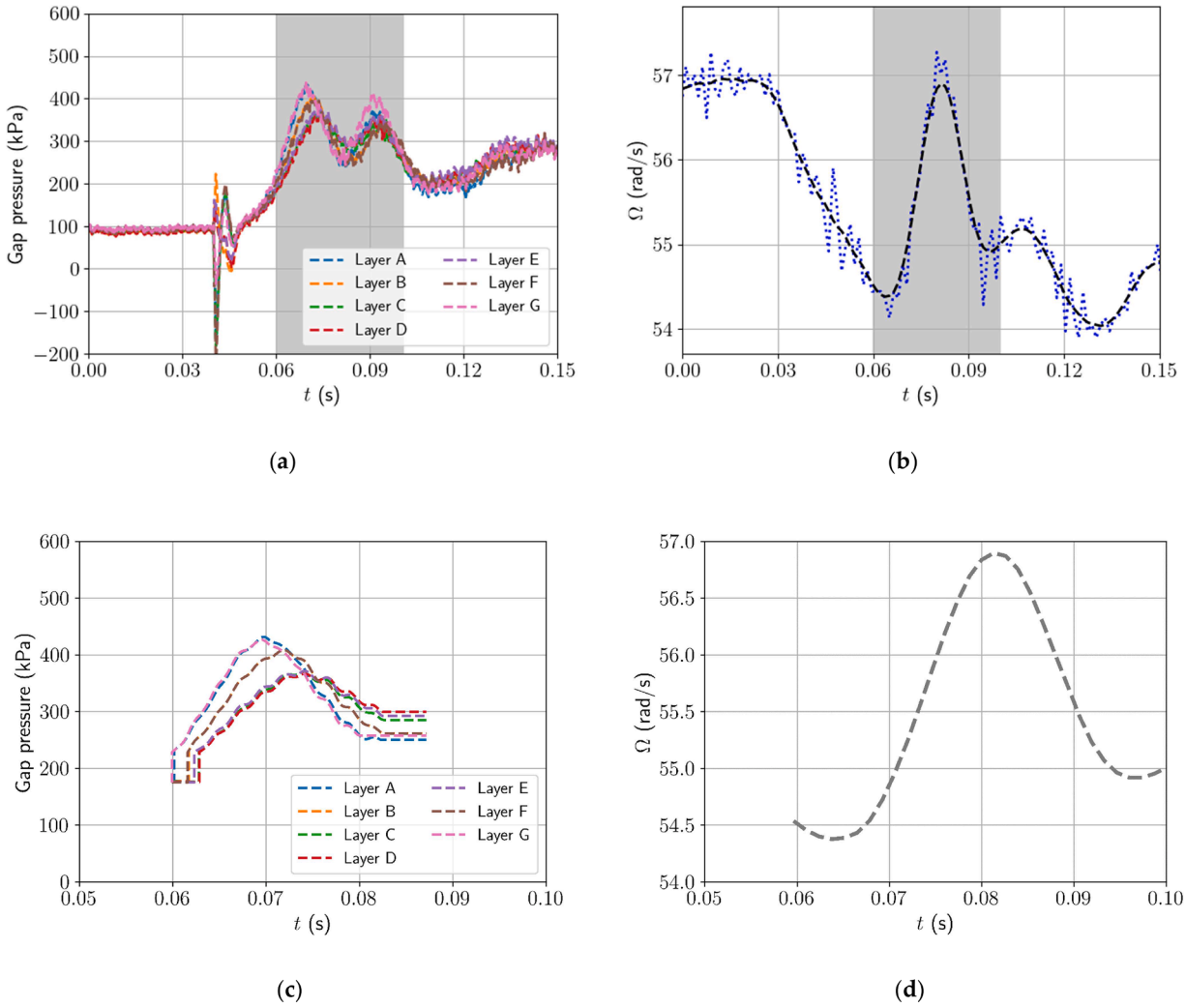

Fig. A2. Gap pressure and rotor speed data for a shaped implosion, shot #897 in Table 3. (**a**) Filtered gap pressure signal (Section 4.1.1) measured in the experiment. (**b**) Rotor speed measured in the experiment. Blue dotted line – raw signal, black dashed line - filtered signal. (**c**) Gap pressure data used as input into simulation. (**d**) Rotor speed data used as input into simulation. Shaded regions in (a) and (b) indicate time range of experimental data used as inputs into simulation. The fluctuation in rotor speed in the experiments is due to the friction (inter-layer seals) and change of the amount of liquid inside the pusher bores during the shot.

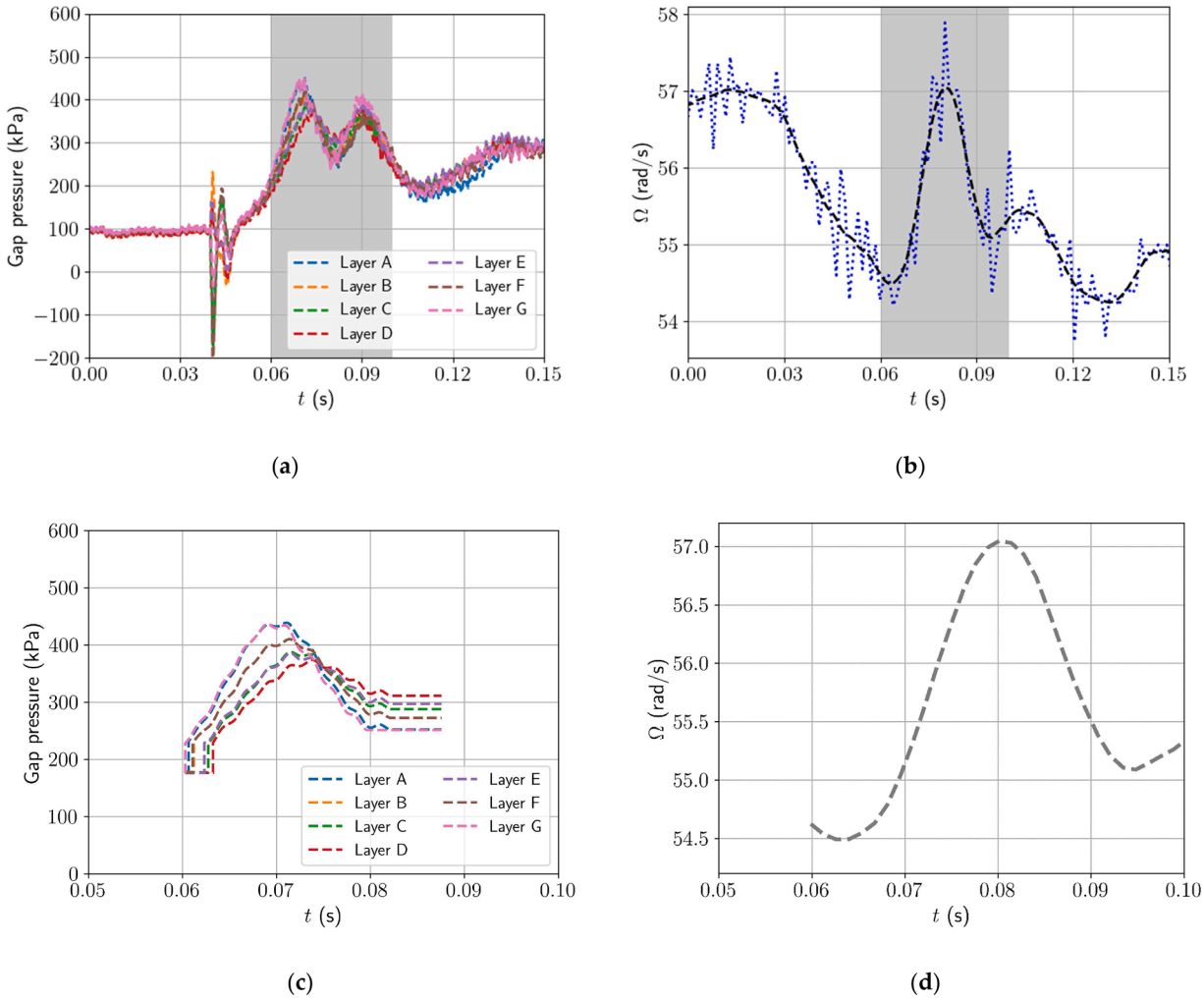

Fig. A3. Gap pressure and rotor speed data for a shaped implosion, shot #898 in Table 3. (**a**) Filtered gap pressure signal (Section 4.1.1) measured in the experiment. (**b**) Rotor speed measured in the experiment. Blue dotted line – raw signal, black dashed line - filtered signal. (**c**) Gap pressure data used as input into simulation. (**d**) Rotor speed data used as input into simulation. Shaded regions in (a) and (b) indicate time range of experimental data used as inputs into simulation. The fluctuation in rotor speed in the experiments is due to the friction (inter-layer seals) and change of the amount of liquid inside the pusher bores during the shot.

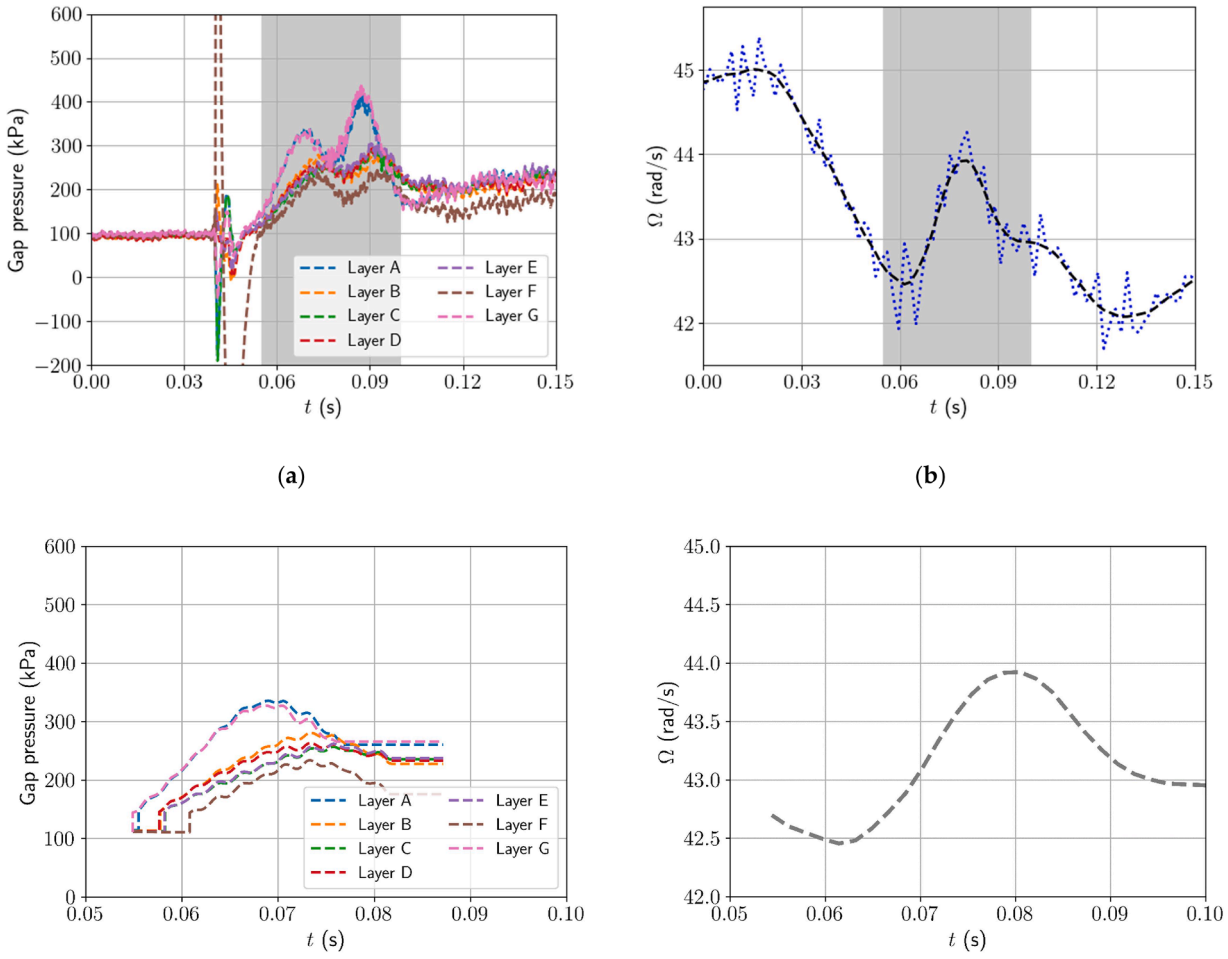

Fig. A4. Gap pressure and rotor speed data for a shaped implosion, shot #899 in Table 3. (**a**) Filtered gap pressure signal (Section 4.1.1) measured in the experiment. (**b**) Rotor speed measured in the experiment. Blue dotted line – raw signal, black dashed line - filtered signal. (**c**) Gap pressure data used as input into simulation. (**d**) Rotor speed data used as input into simulation. Shaded regions in (a) and (b) indicate time range of experimental data used as inputs into simulation. The fluctuation in rotor speed in the experiments is due to the friction (inter-layer seals) and change of the amount of liquid inside the pusher bores during the shot.

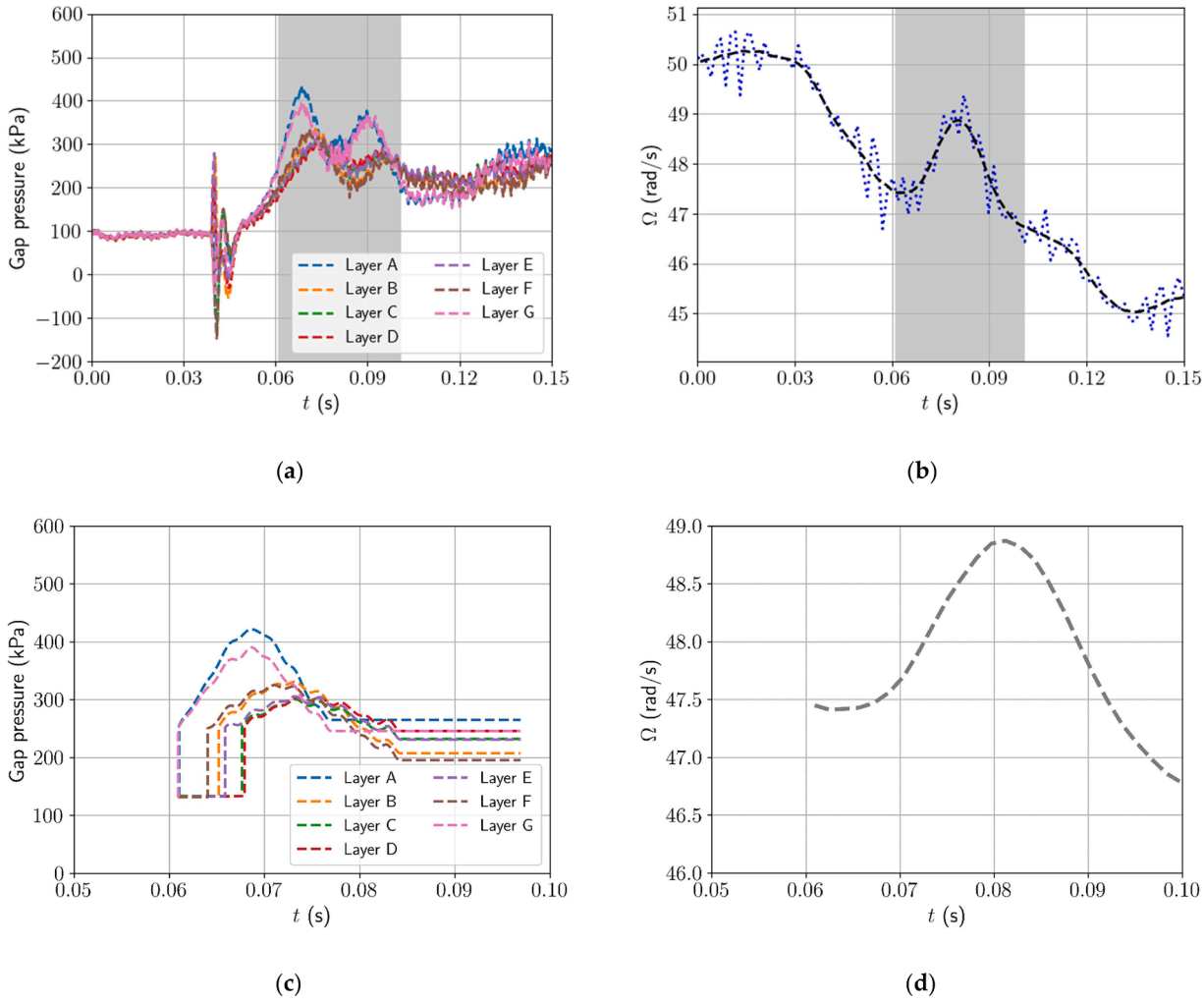

Fig. A5. Gap pressure and rotor speed data for a deep shaped implosion, shot #777 in Table 3. (**a**) Filtered gap pressure signal (Section 4.1.1) measured in the experiment. (**b**) Rotor speed measured in the experiment. Blue dotted line – raw signal, black dashed line - filtered signal. (**c**) Gap pressure data used as input into simulation. (**d**) Rotor speed data used as input into simulation. Shaded regions in (a) and (b) indicate time range of experimental data used as inputs into simulation. The fluctuation in rotor speed in the experiments is due to the friction (inter-layer seals) and change of the amount of liquid inside the pusher bores during the shot.

Appendix B

Table B1
Extended list of parameters for the six selected shots analysed in this work.

Shot number	Shot type	Nominal rotor speed (rad/s)	Initial cavity pressure (kPa)	Accumulator pressure (MPa)		Pusher piston end-stop collisions	Max. radial compression ratio ($C_{rad,\ max}$) at equator	Mean absolute deviation at $C_{rad,\ max}$ at equator (m)
				Layer	Value			
779	Cylindrical	50.3	5.38	A B C D E F G	1.99 1.98 1.98 1.99 1.99 1.99 1.98	No	7.6:1	8×10^{-4}
777* †	Shaped	50.3	5.45	A B C D E F G	2.16 1.16 1.02 0.99 1.02 1.16 2.16	Yes	7.2:1	6×10^{-4}
897	Shaped	57.1	5.45	A B C D E	1.81 1.39 1.22 1.17 1.23	No	5.2:1	3×10^{-4}

(*continued on next page*)

Table B1 (*continued*)

Shot number	Shot type	Nominal rotor speed (rad/s)	Initial cavity pressure (kPa)	Accumulator pressure (MPa)		Pusher piston end-stop collisions	Max. radial compression ratio ($C_{rad,\ max}$) at equator	Mean absolute deviation at $C_{rad,\ max}$ at equator (m)
				Layer	Value			
898	Shaped	57.1	5.45	F G A B C D E F G A	1.36 1.81 1.91 1.49 1.33 1.19 1.33 1.46 1.90 1.72	No	5.7:1	2×10^{-4}
899	Shaped	45.0	8.00	B C D E F G	1.06 0.89 1.02 0.89 1.04 1.72	Yes	5.7:1	11×10^{-4}
849	Cylindrical (RT un-stable)	31.3	102.59	A B C D E F G	2.07 2.07 2.07 2.07 2.07 2.07 2.07	No	2.2:1	9×10^{-4}

* For shot 777 only, driver solenoid valve actuation time was varied between layers, $39.1 \leq t \leq 40.1$ ms.
† For shot 777, pusher pistons experienced higher static friction during launch because it was the first shot in its series.
The measured liquid density for all shots is (990 ± 10) kg/m^3.

Appendix C

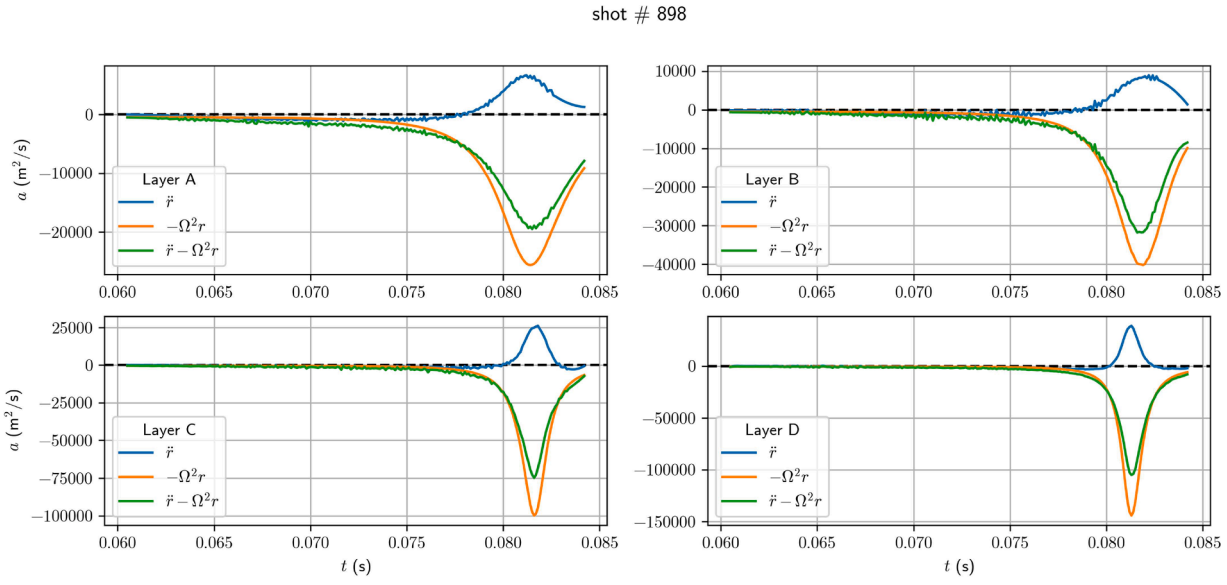

Fig. C1. Acceleration profiles of the inner surface of the liner for RT stable shot #898. The four parts of the figure correspond to radial accelerations extracted at four axial positions: (a) Layer A, (b) Layer B, (c) Layer C, (d) Layer D. Radial acceleration $\frac{d^2r}{dt^2}$ (denoted as $\ddot{r}$) is shown by the blue line. Centripetal acceleration due to liner rotation is shown by the orange line. Total acceleration, which is the sum of radial and centripetal accelerations at the inner surface of the liner, is shown by the green line.

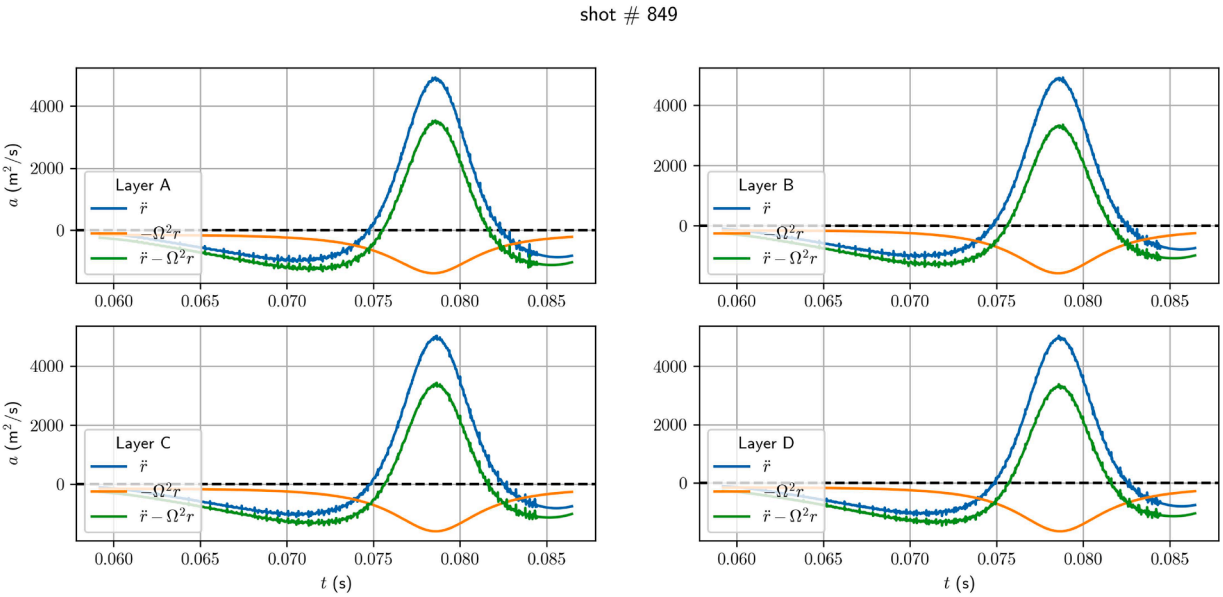

Fig. C2. Acceleration profiles of the inner surface of the liner for RT unstable shot #849. The four parts of the figure correspond to accelerations extracted at four axial positions: (a) Layer A, (b) Layer B, (c) Layer C, (d) Layer D. Radial acceleration $\frac{d^2r}{dt^2}$ (denoted as $\ddot{r}$) is shown by the blue line. Centripetal acceleration due to liner rotation is shown by the orange line. Total acceleration, which is the sum of radial and centripetal accelerations at the inner surface of the liner, is shown by the green line.

A basic criterion for rotational stabilisation of Rayleigh-Taylor instability is for total acceleration to remain negative at all times [23–27]. Total acceleration is the sum of radial and centripetal accelerations. The radial acceleration becomes positive (outward) as the liner decelerates approaching its turnaround point, whilst centripetal acceleration is always negative, and its magnitude increases as the radius of the inner surface of the liner decreases. Therefore, rotation of the liner always has a stabilising effect on the Rayleigh-Taylor instability. Depending on the parameters, rotation can either delay the onset of Rayleigh-Taylor instability and decrease its growth rates, or completely suppress its development. This is illustrated in Figs. C1 and C2 which show acceleration profiles for RT stable (#898) and RT unstable (#849) shots, respectively. One can see that for shot #898, total acceleration remains negative at all times, therefore, development of RT instability is suppressed. On the other hand, for shot #849, the total acceleration becomes positive during the implosion, triggering the onset of Rayleigh-Taylor instability.

References

[1] Bringing fusion energy to market - fusion power, General Fusion, (n.d.). https://generalfusion.com/ (accessed January 16, 2023).

[2] M. Laberge, Magnetized target fusion with a spherical tokamak, J. Fusion Energy 38 (2019) 199–203, https://doi.org/10.1007/S10894-018-0180-3/FIGURES/2.

[3] V. Suponitsky, I. v. Khalzov, E.J. Avital, Magnetohydrodynamics solver for a two-phase free surface flow developed in OpenFOAM, Fluids 7 (2022) 210, https://doi.org/10.3390/FLUIDS7070210. Page7 (2022) 210.

[4] R.C. Kirkpatrick, I.R. Lindemuth, R.E. Reinovsky, P.T. Sheehey, Magnetized target fusion, Curr. Trends Int. Fusion Res. (1997) 543–559, https://doi.org/10.1007/978-1-4615-5867-5_35.

[5] M. Laberge, S. Howard, D. Richardson, A. Froese, V. Suponitsky, M. Reynolds, D. Plant, Acoustically driven magnetized target fusion, in: Proceedings of the IEEE 25th Symposium on Fusion Engineering (SOFE), San Francisco, CA, USA, 2013, https://doi.org/10.1109/SOFE.2013.6635495.

[6] I.R. Lindemuth, R.E. Siemon, R.C. Kirkpatrick, R.E. Reinovsky, Magnetized target fusion (MTF): a low-cost fusion development path, (2004) 289–293. 10.1142/9789812702517_0056.

[7] S. Howard, A. Mossman, W. Zawalski, D. Froese, Plasma-wall interaction on the SLiC spherical tokamak device with large-area, dynamic liquid lithium free surface, in: Proceedings of the 62nd Annual Meeting of the APS Division of Plasma Physics, Bulletin of the American Physical Society, Remote, 2020. https://meetings.aps.org/Meeting/DPP20/Session/GO13.8 (accessed April 4, 2023).

[8] K. Epp, B. Rablah, S. Howard, M. Laberge, M. Reynolds, P. O'Shea, W. Young, P. Carle, A. Froese, R. Ivanov, Recent progress in the PI3 spherical tokamak program, in: Proceedings of the 60th Annual Meeting of the APS Division of Plasma Physics, American Physical Society, Portland, Oregon, USA, 2018. http://meetings.aps.org/link/BAPS.2018.DPP.CP11.192 (accessed April 5, 2023).

[9] A.E. Robson, Linus concept, Ettore Majorana Int. Sci. Ser. Phys. Sci. 13 (1982) 257–279, https://doi.org/10.1007/978-1-4613-3470-5_13/COVER.

[10] Assessment of the slowly-imploding liner (LINUS) fusion reactor concept (Conference) | OSTI.GOV, (n.d.). https://www.osti.gov/biblio/6769582 (accessed January 16, 2023).

[11] Stabilized liner implosions driven by axially-moving free-pistons., (n.d.). https://apps.dtic.mil/sti/citations/ADA042996 (accessed January 16, 2023).

[12] R. Ivanov, W. Young, Plasma studies in the SPECTOR experiment as target development for MTF, Bull. Am. Phys. Soc. 61 (18) (2016). VolumeNumber, http://meetings.aps.org/link/BAPS.2016.DPP.CP10.106 (accessed January 16, 2023).

[13] A. Mossman, M. Laberge, M. Reynolds, S. Howard, C. McNally, L. Carbajal, I. Khalzov, A. Froese, C. Ribeiro, Magnetized target fusion using mechanically-driven liquid metal liner, in: Proceedings of the 64th Annual Meeting of the APS Division of Plasma Physics, Bulletin of the American Physical Society, Spokane, Washington, USA, 2022.

[14] P.J. Turchi, A.L. Cooper, D.J. Jenkins, E.P. Scannell, A LINUS fusion reactor design based on axisymmetric implosion of tangentially-injected liquid metal., 1981. https://apps.dtic.mil/sti/citations/ADA097485 (accessed April 5, 2023).

[15] Groundbreaking Fusion Demonstration Plant | General Fusion, (n.d.). https://generalfusion.com/fusion-demo-plant/ (accessed January 15, 2023).

[16] E.J. Avital, E. Salvatore, A. Munjiza, V. Suponitsky, D. Plant, M. Laberge, Flow design and simulation of a gas compression system for hydrogen fusion energy production, Fluid Dyn. Res. 49 (2017), 045504, https://doi.org/10.1088/1873-7005/AA73BA.

[17] V. Suponitsky, D. Plant, E.J. Avital, A. Munjiza, Pressure wave in liquid generated by pneumatic pistons and its interaction with a free surface, 9 (2017). 10.1142/S1758825117500375.

[18] V. Suponitsky, A. Froese, S. Barsky, Richtmyer–Meshkov instability of a liquid–gas interface driven by a cylindrical imploding pressure wave, Comput. Fluids 89 (2014) 1–19, https://doi.org/10.1016/J.COMPFLUID.2013.10.031.

[19] G. Tóth, A general code for modeling MHD flows on parallel computers: versatile advection code, Astrophys. Lett. Commun. 34 (1996) 245–250, https://doi.org/10.1007/978-94-009-0315-9_101/COVER.

[20] P. Makaremi-Esfariani, P. de Vietien, Coupled CFD/MHD simulations of plasma compression by resistive liquid metal, in: Proceedings of the 62nd Annual Meeting of the APS Division of Plasma Physics, 2020.

[21] A. Barcilon, D.L. Book, A.L. Cooper, Hydrodynamic stability of a rotating liner, Phys. Fluids 17 (2003) 1707, https://doi.org/10.1063/1.1694960.

[22] R. Epstein, On the Bell–Plesset effects: the effects of uniform compression and geometrical convergence on the classical Rayleigh–Taylor instability, Phys. Plasmas 11 (2004) 5114, https://doi.org/10.1063/1.1790496.

[23] K.A. Baldwin, M.M. Scase, R.J.A. Hill, The inhibition of the Rayleigh-Taylor instability by rotation, Sci. Rep. 5 (1) (2015) 1–12, https://doi.org/10.1038/srep11706, 20155.

[24] J. Huneault, D. Plant, A.J. Higgins, Rotational stabilisation of the Rayleigh–Taylor instability at the inner surface of an imploding liquid shell, J. Fluid Mech. 873 (2019) 531–567, https://doi.org/10.1017/JFM.2019.346.
[25] E.J. Avital, V. Suponitsky, I.V. Khalzov, J. Zimmermann, D. Plant, On the hydrodynamic stability of an imploding rotating circular cylindrical liquid liner, Fluid Dyn. Res. 52 (2020), 055505, https://doi.org/10.1088/1873-7005/ABAD8A.
[26] P.J. Turchi, A.L. Cooper, R. Ford, D.J. Jenkins, Rotational stabilization of an imploding liquid cylinder, Phys. Rev. Lett. 36 (1976) 1546, https://doi.org/10.1103/PhysRevLett.36.1546.
[27] D.L. Book, N.K. Winsor, Rotational stabilization of a metallic liner, Phys. Fluids 17 (1974) 662, https://doi.org/10.1063/1.1694772.
[28] G.F. Carnevale, P. Orlandi, Y. Zhou, R.C. Kloosterziel, Rotational suppression of Rayleigh-Taylor instability, J. Fluid Mech. 457 (2002), https://doi.org/10.1017/S0022112002007772.
[29] Y. Zhou, Rayleigh–Taylor and Richtmyer–Meshkov instability induced flow, turbulence, and mixing. I, Phys. Rep. (2017) 720–722, https://doi.org/10.1016/j.physrep.2017.07.005.
[30] Y. Zhou, Rayleigh–Taylor and Richtmyer–Meshkov instability induced flow, turbulence, and mixing. II, Phys. Rep. (2017) 723–725, https://doi.org/10.1016/j.physrep.2017.07.008.
[31] Y. Zhou, T.T. Clark, D.S. Clark, S. Gail Glendinning, M. Aaron Skinner, C. M. Huntington, O.A. Hurricane, A.M. Dimits, B.A. Remington, Turbulent mixing and transition criteria of flows induced by hydrodynamic instabilities, Phys. Plasmas 26 (2019), https://doi.org/10.1063/1.5088745.
[32] D.L. Book, N.K. Winsor, Rotational stabilization of a metallic liner, Phys. Fluids 17 (2003) 662, https://doi.org/10.1063/1.1694772.
[33] H.J. Kull, Theory of the Rayleigh-Taylor instability, Phys. Rep. 206 (1991) 197–325, https://doi.org/10.1016/0370-1573(91)90153-D.
[34] P.J. Turchi, S.D. Frese, M.H. Frese, Stabilized liner compressor for low-cost controlled fusion at megagauss field levels, IEEE Trans. Plasma Sci. 45 (2017) 2800–2809, https://doi.org/10.1109/TPS.2017.2702625.
[35] P.N. Yushmanov, P.N. Yushmanov, T. Takizuka, K.S. Riedel, O.J.W.F. Kardaun, J. G. Cordey, S.M. Kaye, D.E. Post, Scalings for tokamak energy confinement, Nucl. Fusion 30 (1990) 1999, https://doi.org/10.1088/0029-5515/30/10/001.
[36] S.M. Kaye, C.W. Barnes, M.G. Bell, J.C. Deboo, M. Greenwald, K. Riedel, D. Sigmar, N. Uckan, R. Waltz, Status of global energy confinement studies, Phys. Fluids B Plasma Phys. 2 (1998) 2926, https://doi.org/10.1063/1.859578.
[37] I. V. Khalzov, D. Krotez, R. Ségas, An interface tracking, finite volume code for modeling axisymmetric implosion of a rotating liquid metal liner with free surface, Comput. Phys. Commun.. submitted manuscript (2023).
[38] I. V Khalzov, D. Krotez, R. Ségas, ISM-hydro: an interface tracking, finite volume code for modeling axisymmetric implosion of a rotating liquid metal liner with free surface v1.0.0 (Version 1.0.0), Zenodo, October (2023), https://doi.org/10.5281/zenodo.8423698.
[39] P.R.N. Childs, Vorticity and rotation, Rotating Flow (2011) 53–79, https://doi.org/10.1016/B978-0-12-382098-3.00003-2.
[40] D.H. Dolan, Extreme measurements with Photonic Doppler Velocimetry (PDV), Rev. Sci. Instrum. 91 (2020), 051501, https://doi.org/10.1063/5.0004363.
[41] OpenFOAM | Free CFD Software | The OpenFOAM Foundation. https://openfoam.org/(accessed January 16, 2023).
[42] H.G. Weller, A new approach to VOF-based interface capturing methods for incompressible and compressible flow, Technical Report. (2008).
[43] H. Rusche, Computational fluid dynamics of dispersed two-phase flows at high phase fractions, PhD Thesis. 1 (2002).
[44] S.S. Deshpande, L. Anumolu, M.F. Trujillo, Evaluating the performance of the two-phase flow solver interFoam, Comput. Sci. Discov. 5 (2012), https://doi.org/10.1088/1749-4699/5/1/014016.
[45] P.G. Tait, Report on some of the physical properties of fresh water and of sea water, in: Report on the Scientific Results of the Voyage of the H.M.S. Challenger during the Years 1873-76: Physics and Chemistry, 1, Johnson Reprint Corporation, New York, NY, USA, 1965. VolumeAvailable online: https://books.google.ca/books?id=zMgUAQAAIAAJ (accessed on 6 April 2023).
[46] R.W. Moses, R.A. Krakowski, R.L. Miller, Conceptual design of the Fast-Liner Reactor (FLR) for fusion power, (1979). 10.2172/6058274.
[47] Y. Zhou, R.J.R. Williams, P. Ramaprabhu, M. Groom, B. Thornber, A. Hillier, W. Mostert, B. Rollin, S. Balachandar, P.D. Powell, A. Mahalov, N. Attal, Rayleigh–Taylor and Richtmyer–Meshkov instabilities: a journey through scales, Physica D 423 (2021), 132838, https://doi.org/10.1016/J.PHYSD.2020.132838.
[48] P.G. Drazin, W.H. Reid, Hydrodynamic Stability, 2nd ed., Cambridge University Press, 2004 https://doi.org/10.1017/CBO9780511616938.
[49] J. Zimmermann, R. Bouchal, W.R. Smith, Rotating core plasma compression system, WO 2022/155725 A1, 2022.